

Single-Neuron Correlates of Error Monitoring and Post-Error Adjustments in Human Medial Frontal Cortex

Highlights

- Single neurons in the human medial frontal cortex signal self-monitored errors
- Pre-supplementary motor area error signals precede those in anterior cingulate cortex
- Intracranial error-related negativity amplitude correlates with error neuron activity
- iERN amplitude-error neuron spike rate correlation predicts post-error slowing

Authors

Zhongzheng Fu, Daw-An J. Wu,
Ian Ross, Jeffrey M. Chung,
Adam N. Mamelak, Ralph Adolphs,
Ueli Rutishauser

Correspondence

zzbrooks@sfu.edu (Z.F.),
rutishauser@csmc.edu (U.R.)

In Brief

Fu et al. identify single-neuron correlates of error self-monitoring in the human medial frontal cortex. Error neurons respond first in pre-SMA, followed by dACC. The activity of error neurons predicts the amplitude of the error-related negativity trial by trial.



Single-Neuron Correlates of Error Monitoring and Post-Error Adjustments in Human Medial Frontal Cortex

Zhongzheng Fu,^{1,4,8,*} Daw-An J. Wu,³ Ian Ross,⁶ Jeffrey M. Chung,⁷ Adam N. Mamelak,⁸ Ralph Adolphs,^{2,3,5} and Ueli Rutishauser^{2,5,7,8,9,10,*}

¹Division of Engineering and Applied Sciences, California Institute of Technology, Pasadena, CA, USA

²Division of Biology and Biological Engineering, California Institute of Technology, Pasadena, CA, USA

³Division of Humanities and Social Sciences, California Institute of Technology, Pasadena, CA, USA

⁴Control and Dynamical Systems Program, California Institute of Technology, Pasadena, CA, USA

⁵Computation and Neural Systems Program, California Institute of Technology, Pasadena, CA, USA

⁶Department of Neurosurgery, Huntington Memorial Hospital, Pasadena, CA, USA

⁷Department of Neurology, Cedars-Sinai Medical Center, Los Angeles, CA, USA

⁸Department of Neurosurgery, Cedars-Sinai Medical Center, Los Angeles, CA, USA

⁹Center for Neural Science and Medicine, Department of Biomedical Sciences, Cedars-Sinai Medical Center, Los Angeles, CA, USA

¹⁰Lead Contact

*Correspondence: zzbrooks@ucla.edu (Z.F.), rutishauser@csmc.edu (U.R.)

<https://doi.org/10.1016/j.neuron.2018.11.016>

SUMMARY

Humans can self-monitor errors without explicit feedback, resulting in behavioral adjustments on subsequent trials such as post-error slowing (PES). The error-related negativity (ERN) is a well-established macroscopic scalp EEG correlate of error self-monitoring, but its neural origins and relationship to PES remain unknown. We recorded in the frontal cortex of patients performing a Stroop task and found neurons that track self-monitored errors and error history in dorsal anterior cingulate cortex (dACC) and pre-supplementary motor area (pre-SMA). Both the intracranial ERN (iERN) and error neuron responses appeared first in pre-SMA, and ~50 ms later in dACC. Error neuron responses were correlated with iERN amplitude on individual trials. In dACC, such error neuron-iERN synchrony and responses of error-history neurons predicted the magnitude of PES. These data reveal a human single-neuron correlate of the ERN and suggest that dACC synthesizes error information to recruit behavioral control through coordinated neural activity.

INTRODUCTION

A fundamental feature of behavior is the ability to optimize performance based on outcomes (Ullsperger et al., 2014). In humans, performance failure can be monitored not only by explicit external feedback, but also through self-monitoring in the absence of such feedback. Successful detection of errors then initiates behavioral adjustments on various timescales.

These include within-trial adjustment such as online error avoidance (leading to “covert errors”) (Bonini et al., 2014) and immediate correction of the response (Rabbitt, 1966), next-trial adjustment that requires cognitive control such as delaying an impending action (Laming, 1979; Ridderinkhof et al., 2004; Ullsperger et al., 2014), as well as more deliberate adjustments that span several trials to maximize potential rewards (Frank et al., 2005; Quilodran et al., 2008; Shima and Tanji, 1998).

Previous work on identifying the neural substrates for the different components of this behavioral feedback-control loop has revealed that the medial frontal cortex (MFC), which includes the dorsal anterior cingulate cortex (dACC, sometimes also referred to as anterior mid-cingulate cortex [Vogt et al., 2003]) and the pre-supplementary motor area (pre-SMA), serves a critical role for both self-monitoring and control of actions (Ullsperger et al., 2014). While self-monitored errors are robustly signaled by the error-related negativity (ERN) (Gehring et al., 1993; Burle et al., 2008; Godlove et al., 2011; Falkenstein et al., 1991), no single-neuron correlate of this process has yet been reported in humans.

A second large topic concerns the changes in cognitive control that ensue either as a consequence of ongoing prediction of action outcomes, or subsequent to having detected an outcome such as an error. The MFC is also crucially involved in these processes (Kolling et al., 2016; Rushworth and Behrens, 2008; Kerns et al., 2004; Behrens et al., 2007; Brown and Braver, 2005; Shenhav et al., 2013; Sheth et al., 2012; Alexander and Brown, 2011). Such control mechanisms can either trigger switching to a different action based on estimated action values or influence the production of an action, such as delaying an action or adjusting the force with which an action is executed (Gehring et al., 1993; Ullsperger et al., 2014). As an example for the former, MFC neurons encode plans to switch to the alternative action triggered by a reduction of reward (Shima and Tanji, 1998; Williams et al., 2004; Kennerley et al., 2006). Similarly, MFC



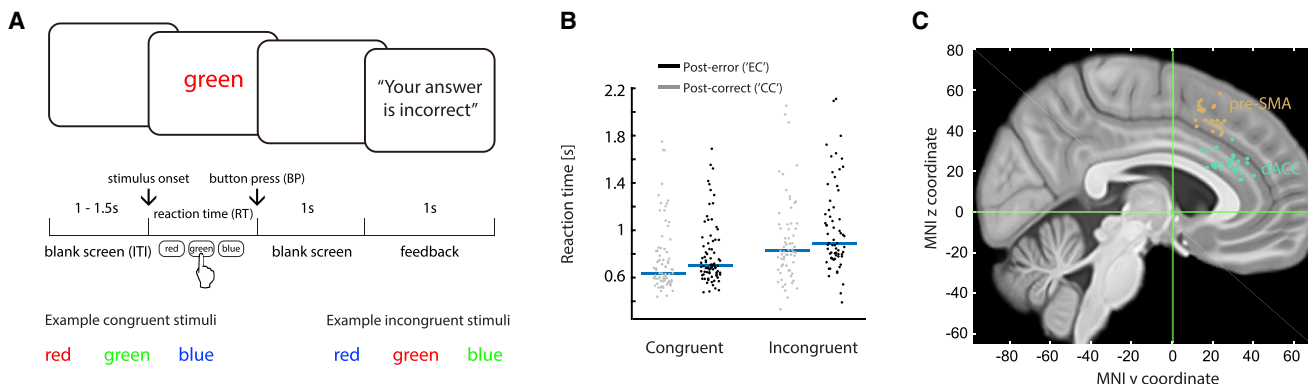


Figure 1. Task, Behavior, and Electrode Localization

(A) Task structure.

(B) Behavior. Each dot represents the mean RT of EC or CC trials of a session.

(C) Recording locations, projected onto the $x = 5$ mm slice. Each dot represents the location of a micro-wire bundle in a patient.

See also Figure S1.

neurons signal the need to switch saccade directions in response to an externally cued rule change (Isoda and Hikosaka, 2007). Lesioning or pharmacological manipulation of the MFC disrupts such reward history-dependent alternative action selection (Shima and Tanji, 1998; Kennerley et al., 2006), illustrating a critical role for the MFC in explore-exploit decisions.

Less is known about the MFC's involvement in control of action production triggered by monitored outcomes (mentioned above as the second type of behavioral adjustments). In the case of externally cued response inhibition, electrical stimulation of the supplementary eye field or pre-SMA has been shown to delay saccades in service of avoiding errors (Stuphorn and Schall, 2006; Isoda and Hikosaka, 2007). These studies provide crucial causal evidence that MFC can influence action production, but the neuronal mechanisms that bridge monitoring to such control and the possible roles of other brain regions in this process remain unclear. Self-monitored errors, on the other hand, have a typical behavioral consequence: they can delay successive actions, a phenomenon known as the post-error slowing (PES) (Ullsperger et al., 2014). Functional imaging studies have revealed the complex neural mechanism that may underlie PES with MFC being the central node of this control network. In this framework, the need for PES is signaled by MFC after detection of an error. PES involves inhibitory activity in the cortico-subthalamic pathways (Danielmeier et al., 2011; Aron and Poldrack, 2006; Aron et al., 2007), as well as adaptations in motor cortex (Danielmeier et al., 2011) and sensory processing and integration regions (Purcell and Kiani, 2016; Ullsperger and Danielmeier, 2016; King et al., 2010). This argument is principally supported by the finding that blood-oxygen-level-dependent (BOLD) activation in dACC is correlated with the magnitude of PES (Kerns et al., 2004). In addition, in rodents, pharmacological inactivation of MFC abolishes PES (Narayanan et al., 2013).

A natural hypothesis thus links the detection of self-generated errors, as reflected in the ERN, with changes in cognitive control, as exhibited behaviorally in PES, predicting that the two measures should be correlated. However, several electroencephalogram (EEG) studies have failed to find a significant relationship

between PES and ERN (Gehring and Fencsik, 2001; Nieuwenhuis et al., 2001; Hajcak et al., 2003). Curiously, while BOLD activity in MFC predicts PES, the ERN does not. Based on these discrepancies in the literature, we tested a more detailed mechanistic hypothesis that might reconcile them. The ERN is thought to be produced by the summation of postsynaptic potentials within MFC and may thus, in part, reflect inputs to this region (Holroyd and Coles, 2002; Luck, 2014). One possibility explaining the aforementioned discrepancies is that the inputs to the MFC that produce the ERN only carry information about error monitoring, but not about the engagement of control. The computations within MFC that underlie cognitive control, while not reflected in the ERN, might instead be evident in oscillatory components in the local field potential (LFP) (Siegel et al., 2012; Pesaran et al., 2018) or in correlations between spike rates of neurons and the LFP (Nir et al., 2007). Such correlated neuronal activity could also explain why BOLD signals are associated with PES (Niessing et al., 2005). This model predicts that spike rates and intracranial EEG (iEEG) power within MFC would be correlated with the strength of PES, even though the ERN is not.

RESULTS

Task and Behavior

Subjects performed a color-naming Stroop task, which required subjects to name the color of words while ignoring their semantic meaning (Figure 1A). Reaction times (RTs) were longer on word-color incongruent trials than word-color congruent trials (the "Stroop effect"; 224.9 ± 19.2 ms difference, mean \pm SEM across sessions, $F(1, 84) = 116.6$, $p < 0.001$, mixed-effects one-way ANOVA). Subjects responded incorrectly ("error trials") in $7.2\% \pm 0.5\%$ (\pm SEM) of all trials. On correct trials that follow an error ("EC" trials), responses were significantly slower than on correct trials that follow another correct trial ("CC" trials) (Figure 1B, amount of PES: 64.3 ± 11.0 ms, mean \pm SEM across sessions, mixed-effect one-way ANOVA, $F(1, 184) = 23.4$, $p < 0.001$). To quantify PES for individual trials in the analysis below, we used sequences of CCEC trials ('C' represents correct trials;

'E' represents error trials; see **STAR Methods**; median single-trial PES = 33 ms, $p = 0.0016$, $z = 3.154$; signed-rank test).

Single-Neuron Correlates of Error Self-Monitoring

We isolated 1,171 single units from dACC ($n = 618$) and pre-SMA ($n = 553$) across 29 patients (Figure 1C, Table S1; see also Figures S1A–S1C and S1D–S1I). Some neurons were in sessions with fewer than seven error trials and thus were excluded from the analyses that involve errors (number of neurons included in dACC is $n = 399$ and in pre-SMA is $n = 431$). Error neurons were identified using a Poisson regression model. Spike rates in a 1-s epoch starting immediately after the action (button press) were regressed against trial labels (error or correct) and RTs. 34% ($n = 134$) of dACC and 46% ($n = 198$) of pre-SMA neurons signaled errors (see Figures 2A–2D, 3A–3C, S2C, and S2D and Table S2). We classified error neurons based on whether they had higher ("type I," error > correct, $n = 99$ and 118 in dACC and pre-SMA, respectively; see Figures 2A, 2C, 3B, and 3C, left) or lower ("type II," error < correct, $n = 35$ and 80 in dACC and pre-SMA, respectively, Figures 2B, 2D, 3B, and 3C, right) spike rates for error than correct trials. The responses of error neurons on individual trials differed reliably between error and correct trials as evaluated using receiver-operating characteristic (ROC) analysis (see **STAR Methods** and Figure 3F): area under the curve (AUC) values were, on average, 0.61 and 0.60 for dACC and pre-SMA, respectively (significantly greater than 0.5 with $p < 10^{-10}$, $t(133) = 12.86$ and $p < 10^{-10}$, $t(197) = 18.5$, respectively; t test). AUC values of error neurons did not differ significantly between dACC and pre-SMA (Figure 3F; $p = 0.52$, $t(330) = 0.64$, t test).

The majority of errors (67%) occurred on incongruent trials. Spike rates of error neurons on the error trials (within the post-action epoch; Figure S2A) did not correlate with RT (Figures S3A and S3B; for type I error neurons, $p > 0.4$, $t(98) = 0.86$ in dACC, $p > 0.5$, $t(117) = -0.41$ in pre-SMA; for type II error neurons, $p > 0.5$, $t(34) = -0.54$ in dACC and $p > 0.5$, $t(79) = -0.63$ in pre-SMA; t test) and did not distinguish significantly between congruent and incongruent errors (Figures S4A and S4C; see Figures S4B and S4D for statistics). We thus pooled congruent and incongruent error trials in all subsequent analyses. Unlike the responses of error neurons, RTs were significantly longer on incongruent compared to congruent error trials (Figure S4G; $p < 0.001$, $t(57) = 4.03$, paired t test), arguing that errors were not due to lapses in stimulus processing.

While the neuronal error signal persisted into the post-feedback epoch (which appeared 1 s after button press; Figures 1A and S2A), the maximal spike rate modulation for both types of error neurons occurred before onset of feedback (Figures 3B and 3C). An out-of-sample analysis of effect sizes (see **STAR Methods**) confirmed this impression: spike rates of error neurons in the epoch between action and feedback onset carried significantly more information about the occurrence of an error than those in the post-feedback epoch (Figure 3G; $p < 10^{-10}$, $t(199) = 98.3$ in dACC, $p < 10^{-10}$, $t(199) = 288.2$ in pre-SMA, paired t test). Thus, feedback onset did not reactivate error neurons or terminate their ongoing response on error trials (Figures 3B and 3C). In summary, error neurons were action-triggered and encoded the detection of a mismatch between the intended action and the actual action performed.

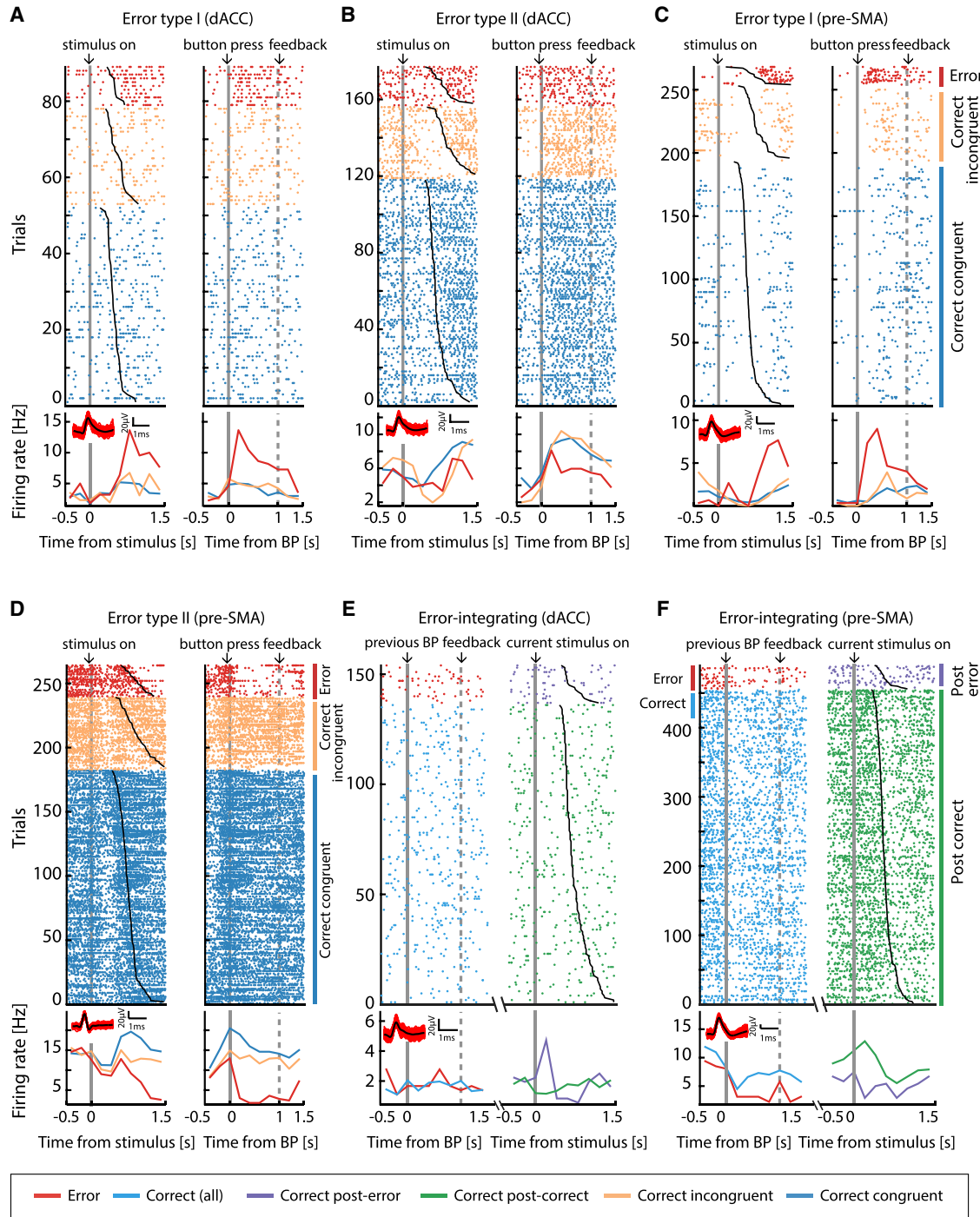
Error-Integrating Neurons

We hypothesized that MFC neurons signal information about the history of self-monitored outcomes (Shima and Tanji, 1998; Kennerley et al., 2006). We identified a significant proportion of MFC neurons (see Figure 3A; $n = 46$, 11.5% in the dACC; $n = 58$, 13.5% in pre-SMA, $p < 0.001$ for both areas, permutation test; also see Table S2) whose spike rates signaled whether the response in the preceding trial was an error or not (Figures 2E, 2F, 3A, S2C, and S2D). Response patterns of these "error-integrating" neurons differed between dACC and pre-SMA: whereas dACC neurons (Figure 3D) showed a peri-stimulus onset spike rate increase on trials that followed an error, responses in pre-SMA were characterized by an extended decrease starting in the pre-stimulus baseline period (Figure 3E).

We next tested whether this response pattern was the result of error signals persisting from the preceding error trial, in which case the error-integrating neurons would also be classified as error neurons. While there was some overlap between the two categories (overlap: $n = 12$ and 20 for dACC and pre-SMA), many error-integrating neurons were not also error neurons (non-overlap: $n = 34$ and $n = 38$ for dACC and pre-SMA, respectively). The time course of the population activity of all error-integrating neurons confirmed this: while these neurons did signal errors to some degree during the post-action epoch (definition see Figure S2) on the preceding trial (Figure 3H, orange; mean AUC for dACC 0.59 ± 0.01 , for pre-SMA 0.63 ± 0.01 ; $p < 0.05$ versus chance for both areas, permutation tests), this error signal was attenuated after feedback (Figure 3H, green; mean AUC for dACC 0.59 ± 0.01 , for pre-SMA 0.57 ± 0.01), reinforced before stimulus onset, and then continued on to after the stimulus onset on the next correct trial (Figure 3H, blue; mean AUC for dACC 0.65 ± 0.01 , for pre-SMA 0.62 ± 0.01 ; blue versus green, $p < 0.001$, $z = 4.74$ in dACC and $p < 0.001$, $z = 4.72$ in pre-SMA, rank-sum test). In summary, we found error-integrating neurons carried a sustained error signal that was reinforced around stimulus onset on the subsequent trial, consistent with a putative role in post-error behavioral control.

Relationship between Error and Conflict Neurons, and a Signature of Control

Response conflict is thought to be the stimulus-evoked competition between a pre-potent but task-irrelevant response (reading the word) and a task-relevant response (the ink color) (Botvinick et al., 2001; Shenhav et al., 2013). In this framework, error signals are generated by conflict between the committed erroneous response and continuing development of the correct response. This implies that error neurons should not only signal errors, but also signal conflict as soon as it arises following stimulus onset. Here, we tested this hypothesis. We found that, as a group, the spike rates of error neurons within the post-stimulus epoch ([0 500]ms relative to stimulus onset; Figure S2A) did not distinguish significantly between incongruent and congruent stimuli (Figures S3C and S3D; see legend for statistics). For the second analysis, we first identified conflict neurons in both dACC (Figure S3E; $p = 0.03$, $n = 41$, 6.7% of recorded neurons for type I and $p < 0.001$, $n = 43$, 7% of recorded neurons for type II; permutation tests)

**Figure 2. Examples of Error and Error-Integrating Neurons**

(A–D) Error neurons.

(E and F) Error-integrating neurons.

(A–F) Raster (top) and mean spike rates (bottom) aligned at stimulus onset (left) and button press (right; BP) for (A)–(D), aligned to previous-trial button press (left) and to current-trial stimulus onset (right) for (E) and (F). Trials are sorted by reaction time (RT) (black line overlaying raster plots) and trial types (color; from top to bottom, error, correct incongruent, correct congruent for (A)–(D); EC and CC trials for E and F). Solid gray bars, time points for alignments. Broken gray bars, onset of feedback. Insets show the waveforms associated with each neuron and the corresponding scale bars.

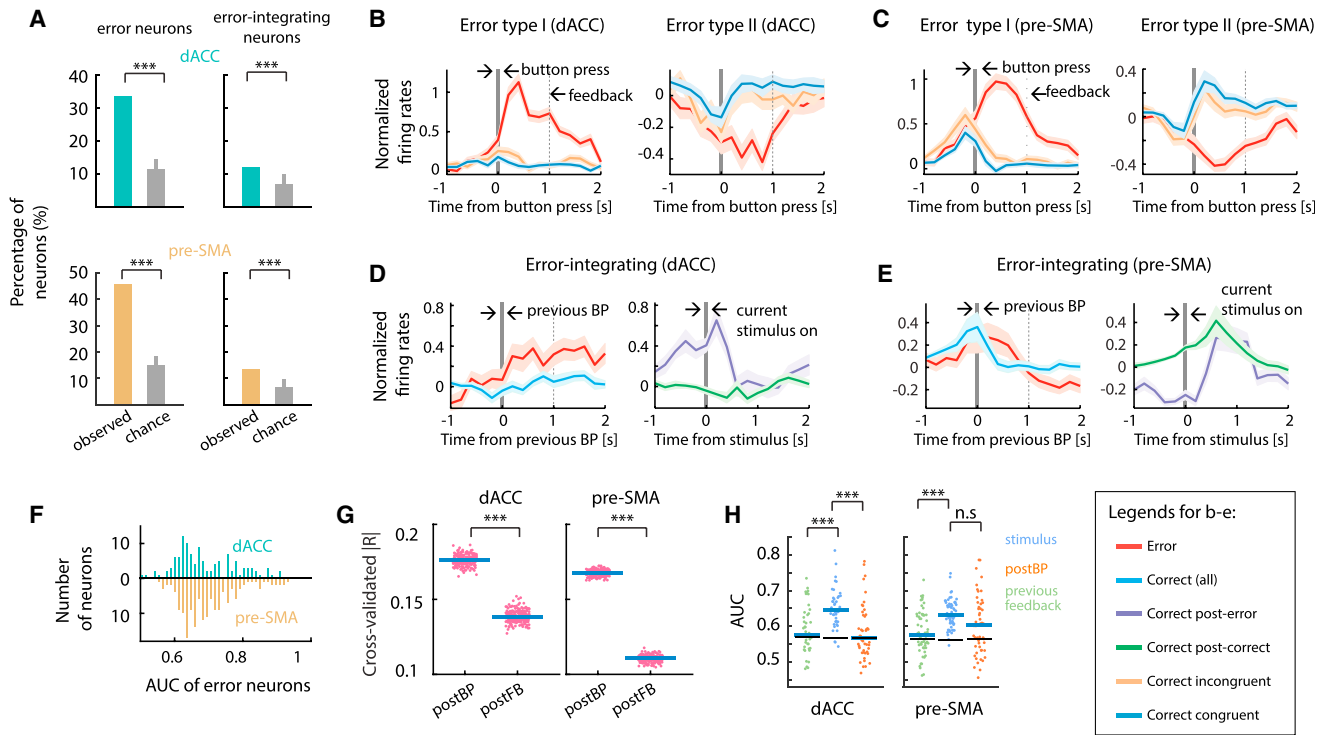


Figure 3. Temporal Profile of Error and Error-Integrating Neurons

(A) Percentage of significant error and error-integrating neurons in dACC and pre-SMA. Gray bar is null distribution (mean and 95% confidence interval). (B) Average standardized spike rates for all dACC error neurons, aligned at button press ($t = 0$, gray bar). Broken bars, 1 s after button press. Shading is \pm SEM across neurons. (C) Same as (B), but for pre-SMA error neurons. (D) Average standardized spike rates as a function of time for dACC error-integrating neurons, aligned at preceding-trial button press (left) or current-trial stimulus onset (right). (E) Same as (D) but for the pre-SMA. (F) Receiver-operating characteristic (ROC) analysis. Error signal can be reliably decoded at the single-trial level (type I and type II error neurons pooled). (G) Statistics for (B and C). Error neurons distinguished between error and correct trials more strongly after button press compared to after onset of feedback. Shown are cross-validated partial correlation coefficients across all error neurons (type I and II pooled). Each data point represents the mean effect size across all error neurons in one cross-validation run. (H) Statistics for (D) and (E). ROC analysis of the response of error-integrating neurons in three different time windows. The spike rates of error-integrating neurons differentiated between EC and CC trials in the current-trial peri-stimulus time window (blue; [-500 500]ms relative to stimulus onset) significantly better than those in the preceding-trial post-feedback period in differentiating between error and correct trials. Error bars, \pm SEM across neurons. Broken horizontal lines, the 97.5th percentile of the null distribution.

* $p < 0.05$, ** $p \leq 0.01$, *** $p \leq 0.001$. n.s., not significant ($p > 0.05$). BP, button press.

and pre-SMA ($p < 0.001$, $n = 54$, 10%, type I only; permutation test), confirming earlier work (Sheth et al., 2012; Ebitz and Platt, 2015). These neurons changed their spike rates to signal conflict, with the signal culminating \sim 500 ms after stimulus onset (Figure S3F). The majority of error neurons were not conflict neurons (81% of error neurons in dACC and 87% of error neurons in pre-SMA were not conflict neurons) and vice versa (Table S3). The number of neurons that qualified as both error and conflict neurons was not significantly greater than what was expected if these two categories were independent (Fisher's exact test for association; see Table S3). Also, error neurons are significantly more common in MFC relative to conflict neurons (28% versus 12%, $p < 0.001$, $\chi^2(1) = 93.64$, chi-square test). Thus, the substrates for error monitoring and conflict detection are largely separated at the neuronal level.

According to the model mentioned above, on an incongruent and correct trial, conflict arises accompanying stimulus onset and recruits cognitive control, which in turn resolves the conflict and results in a correct response. Neural activity reflecting conflict detection and the state of cognitive control is thus intermingled. To separate them, we compared spike rates within the post-stimulus epoch between error incongruent and correct incongruent trials for the previously identified groups of neurons. We found that, at the group level, only type II error neurons in dACC (Figure S3G) as well as conflict neurons in both dACC (Figures S3J and S3K) and pre-SMA (Figure S3L) carry a signature of control state according to this metric (see legend for statistics). We also confirmed these results by a multi-level Poisson regression model where the RT effect is controlled, with qualitatively similar results (data not shown). None of the other types of neurons changed their spike rates significantly to reflect the control state

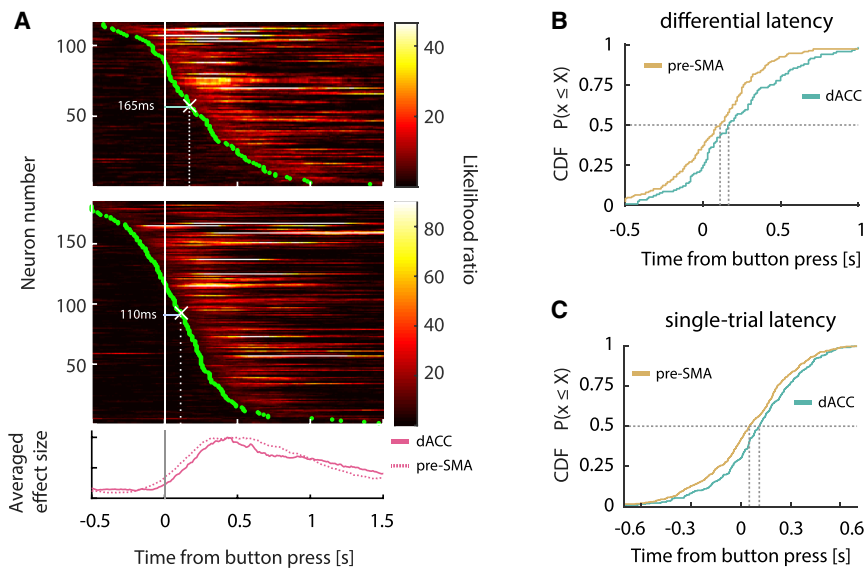


Figure 4. Error Neurons in Pre-SMA Respond Earlier Than Error Neurons in dACC

(A) Temporal profile of error information carried by the error neuronal population (type I and II pooled), aligned at button press (gray bar) and sorted by the onset latencies of error information (green dots). Each row represents one error neuron in dACC (upper) or pre-SMA (middle). White crosses mark the medians of onset latencies. Bottom plot shows the average likelihood ratio normalized by the peak value (solid line, dACC; broken lines, pre-SMA).

(B) CDF of differential latencies (see STAR Methods for details) are shown for error neurons.

(C) CDF of single-trial onset latencies for error neurons.

CDF, cumulative distribution function.

($p = 0.41$, $z = 0.82$ for type I error neuron in dACC; $p = 0.87$, z value = 0.16 for type I error neuron and $p = 0.26$, $z = -1.12$ for type II error neuron in pre-SMA; $p = 0.17$, $z = -1.37$ for error-integrating neurons in dACC, $p = 0.24$, $z = -1.16$ for error integrating neurons in pre-SMA; signed-rank test). Notably, the type I error neurons and error-integrating neurons in both dACC and pre-SMA did not carry this signature of control state, consistent with a more specialized role in monitoring and control, respectively.

Waveforms of Error Neurons and Error-Integrating Neurons

We quantified the duration of the extracellular waveforms of neurons (“trough-to-peak time”) to differentiate between putative cell types (Barthó et al., 2004; Mitchell et al., 2007; Rutishauser et al., 2015). The distribution of spike duration is significantly bimodal in both dACC and pre-SMA (Figures S5A and S5E; $p < 0.001$ for both areas, Hartigan’s dip test). 80% of neurons had broad waveforms (trough-to-peak time greater than 0.5 ms), a feature indicative of putative pyramidal cells (Mitchell et al., 2007). Comparing the proportion of putative pyramidal and inhibitory neurons within each category with the overall population revealed that most error and error-integrating neurons are putatively excitatory (see Figure S5 legend for statistics).

Error Neurons Signal Errors Earlier in pre-SMA Than in dACC

We next sought the point in time when error information first became available in each brain region. We first estimated the differential onset latency (the first point in time when the spike rates significantly differentiated between two conditions, see STAR Methods), which showed that the error signal in pre-SMA occurred significantly earlier than in dACC by 55 ms (Figures 4A and 4B; median dACC latency, 165 ms; median pre-SMA latency, 110 ms; $p = 0.002$ and $z = 3.05$, rank-sum test). A putative downstream readout (here a decoder), however, only has access to the response of an error neuron on a single trial.

We used a Poisson-based method to detect, for each trial, the point of time the spike rate of a given error neuron departed significantly from the baseline (type I only; see STAR Methods for details). This analysis revealed that the error signal appeared first in pre-SMA 52 ms after button press (Figure 4C; $p = 0.0025$, $z = 3.02$, rank-sum test), followed by the response in the dACC 60 ms later (median difference). Repeating this analysis restricting to simultaneously recorded error neurons revealed quantitatively similar results ($p = 0.002$ and $z = 2.89$; one-tailed rank-sum tests).

Error-Related Negativity

Simultaneously with single neurons, we recorded the iEEG using low-impedance macro contacts in both dACC and pre-SMA (see Table S1 and Figure S1A). Following an erroneous button press, the iEEG revealed a prominent intracranial ERN (iERN) visible on single trials in both dACC and pre-SMA (Figures 5A–5C, S6A, and S6B). We also repeated the same task with scalp EEG in control subjects (see STAR Methods) and found that the scalp ERN (Figures S6C and S6D) had waveforms similar to the iERN, but with 5–10 times smaller amplitude (cf. Figures 5C and S6C). The extracted iERN amplitude values significantly distinguished error from correct trials (see STAR Methods for details; Figure 5D; median AUC for dACC electrodes is 0.59, $p < 10^{-10}$, $z = 7.72$; median AUC for pre-SMA electrodes is 0.67, $p < 10^{-10}$, $z = 7.78$; signed-rank test).

Time-frequency analyses revealed that iEEG power increased following button press in two frequency bands: 2–5 Hz (“slow theta”) and 5–10 Hz (“theta”) on both error and correct trials (Figure 5E), with a significantly stronger increase on error trials (Figures S6E and S6F; see legend for statistics). Previous studies have demonstrated that volume conduction from the hippocampus can account for theta oscillations in neocortex (Sirota et al., 2008; Gerbrandt et al., 1978). For this reason, we next repeated the same analysis for simultaneously recorded hippocampal iEEG. Although there were significant differences between error and correct trials, the differences were of opposite sign (Figures S6E

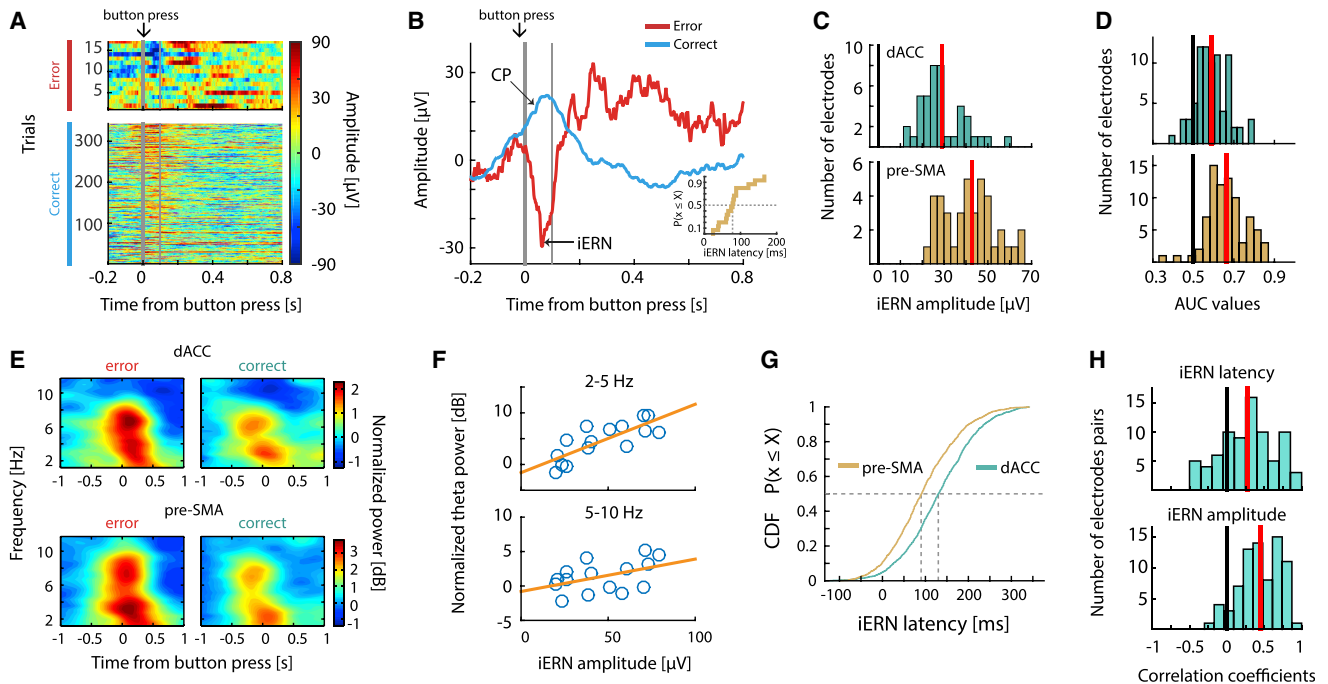


Figure 5. Intracranial Error-Related Negativity

- (A) Example single-trial event-related potentials recorded from dACC, sorted by RT (RT increases from top to bottom rows) and trial types. $t = 0$ is button press. Thin vertical bar marks 100 ms after button press.
- (B) Average of data shown in (A) grouped by trial types (colors; red for error, blue for correct), aligned at button press ($t = 0$, thick vertical gray bar). Inset, distribution of iERN latencies for the same data. Thin vertical bar marks 100 ms after button press.
- (C) Mean iERN amplitudes over all electrodes placed in dACC (green) and pre-SMA (brown). Red vertical bars show the median values.
- (D) iERN amplitudes differ significantly between correct and error trials, evaluated using ROC analysis (see main text for details). Red vertical bars show the mean values.
- (E) Spectral signature of the error signal. The power spectrum is aligned at button press ($t = 0$; averaged across $n = 42$ sessions). The region of power increase visibly splits into two frequency bands (2–5 and 5–10 Hz). See Figures S6E and S6F for statistics.
- (F) Trial-by-trial correlation between iERN amplitude and slow-theta (2–5 Hz; top) and (5–10 Hz; bottom) power for the example session shown in (A) and (B).
- (G) Comparison of iERN latency across all sessions. The iERN peak occurred significantly earlier in the pre-SMA compared to the dACC.
- (H) Trial-by-trial correlation of iERN latency (upper) and iERN amplitude (lower) between pairs of iERNs recorded simultaneously in dACC and pre-SMA. For both, the correlation coefficients have a mean significantly greater than zero. Red vertical bars show the mean values.

and S6F; see legend for statistics), suggesting that the signals we reported in MFC are not volume conducted from the hippocampus.

A power increase in both bands (averaged within $[-0.5$ s, $+0.5$ s] around button press) was correlated with the iERN peak amplitude on the same trial (Figure 5F shows this relationship for the data in Figures 5A and 5B; Figures S6G and S6H show population summary; for theta-iERN correlation, mean correlation = 0.33, $p < 10^{-10}$, $t(78) = 12.15$ in dACC and mean correlation = 0.41, $p < 10^{-10}$, $t(79) = 16.52$ in pre-SMA; for slow theta-iERN correlation, mean correlation = 0.44, $p < 10^{-10}$, $t(78) = 19.2$; mean correlation = 0.48, $p < 10^{-10}$, $t(79) = 19.4$ in pre-SMA; mean-versus-zero comparisons, t test). The ERN is thought to contain a combination of phase-locked theta-frequency-band activity and non-phase-locked theta-frequency-band power increases (Yeung et al., 2007; Trujillo and Allen, 2007; Wang et al., 2005; Luu et al., 2004). Induced theta power (Figure S6I) alone in the same time-frequency region of interest was also significantly correlated with iERN amplitude (Figures S6J and S6K; see legend for statistics).

Consistent with the spiking activity of error neurons reported above, the iERN amplitude, theta, and slow theta power also did not differ significantly between congruent and incongruent errors (Figures S4E and S4F; see legend for statistics). Although the iERN in dACC and pre-SMA had similar waveforms, their peak latency differed: the iERN occurred on average 40 ms earlier in pre-SMA than in dACC (Figure 5G; For a comparison with spike latency, see Figure S6N; median dACC latency is 140 ms, median pre-SMA latency is 100 ms; $p < 10^{-10}$, $z = 13.04$, rank-sum test; this effect held even after equalizing amplitudes across areas, $p < 10^{-10}$, $z = 10.5$, rank-sum test). We also investigated the difference as well as correlation in latency and amplitude between pairs of simultaneously recorded iERNs. The distribution of these latency difference values between the iERN pairs have a significantly non-zero median (Figure S6L; median = 18 ms; $p < 0.001$, $z = 19.27$, rank-sum test), further confirming the leading role of pre-SMA. This latency difference also provides evidence against the hypothesis that the iERN is volume conducted because this would result in simultaneous onset (Logothetis et al., 2007). Similarly, the amplitude difference

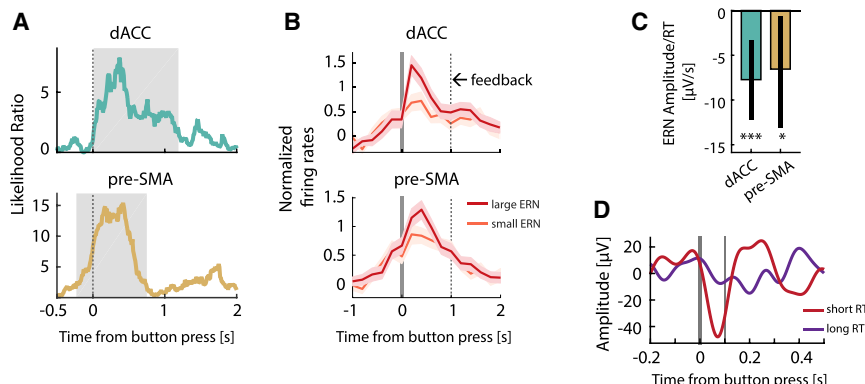


Figure 6. The iERN Amplitude Is Correlated with Error Neuron Spike Rate and RT
(A) iERN amplitude correlated significantly with the spike rates of error neurons (type I). The likelihood ratio peaked around ~400 ms after button press. $t = 0$ is button press. Gray shading delineates the extent of the significant cluster as determined by a cluster-based permutation test. Note that the significant cluster started earlier in pre-SMA.

(B) Illustration of the relationship between RT and iERN amplitude (data from one session). iERN amplitudes were larger when the corresponding RTs were short (red; RTs shorter than the median) than when RTs were long (purple; RTs longer than the median). Thick vertical bar marks button press; thin vertical bar marks 100 ms after button press. See (C) for statistics.

* $p \leq 0.05$, ** $p \leq 0.01$, *** $p \leq 0.001$.

between iERN pairs was significantly positive (Figure S6M; median = 11 μV ; $p < 0.001$, $z = 20.14$, rank-sum test). In addition, both the latency and amplitudes of pairs are significantly correlated (Figure 5H; mean correlation coefficient for latency correlation is 0.27 and for amplitude correlation is 0.44; $p < 0.001$, $t(77) = 6.81$ for latency correlation and $p < 0.001$, $t(77) = 0.29$ for amplitude correlation, t test). Together, these data show that the iERN is accompanied by theta and slow theta activity in MFC, and that the iERNs appeared earlier and with larger amplitude in pre-SMA.

Linking Spikes, iERN, and Behavior

To gain insights into the processes that contribute to the iERN, we began by correlating its amplitude with the spike rates of error neurons. We used a multi-level linear model in which iERN amplitude was the dependent variable, and RT and spike rates were fixed effects. We then tested whether this model explained the data significantly better than a null model (see STAR Methods). Here, the null model has the iERN amplitude as the dependent variable, and only RT as the fixed effect (and all the random effects remained the same as before). Note that only error trials were included in this analysis. The spike rates of type I error neurons significantly co-varied with the iERN amplitude recorded in the same brain region in a trial-by-trial fashion (Figure 6A, $p = 0.01$ for dACC error neurons, $p < 0.001$ for pre-SMA error neurons; cluster-based permutation test for the time course, details see STAR Methods). This effect was evident at the single-cell level: each error neuron's mean spike rate was greatest on trials with the largest iERN amplitude (Figure 6B). This correlation began around action onset (button press), peaked ~400 ms after erroneous actions with a maximal likelihood ratio of 7.9 for dACC and 15.4 for pre-SMA, and occurred earlier in pre-SMA compared to dACC (Figure 6A). This is consistent with the shorter iERN latencies in pre-SMA reported above (Figure 5G). This effect held when we used spike counts within the post-action epoch ([0–1]s after button press; Figure S7A; $p =$

0.008, $\chi^2(1) = 6.56$ in dACC and $p = 0.012$, $\chi^2(1) = 5.81$ in pre-SMA). We found no significant correlation between iERN amplitude and spike rates of type II error neurons (Figure S7B; spike counts within [0–1]s after button press were used in the GLM; $p = 0.19$, $\chi^2(1) = 1.64$ in dACC, $p = 0.07$, $\chi^2(1) = 3.36$ in pre-SMA, likelihood ratio test) or non-error neurons ($p > 0.1$, cluster-based permutation test).

Does the same relationship hold on correct trials? To answer this question, we first extracted the positive peaks on the correct trials as informed by the average event-related potential (ERP) shape (Figure 5B, see STAR Methods). We then constructed a similar multi-level model but with evoked potentials on the correct trial ("CP") as the response variable, and spike rates of error neurons and RT on the same trial as fixed effects. We found no significant correlation between the evoked potential amplitude and spike rates of error neurons on correct trials (Figure S7C; $p = 0.34$, $\chi^2(1) = 0.92$ for type I error neurons and $p = 0.74$, $\chi^2(1) = 0.11$ for type II error neurons in dACC; $p = 0.88$, $\chi^2(1) = 0.023$ for type I error neurons and $p = 0.74$, $\chi^2(1) = 0.11$ for type II error neurons in pre-SMA). The relationship between spiking activity and amplitude of evoked potential is thus specific to error neurons.

Each trial was characterized not only by whether an error occurred (indexed by error neurons), but also by its RT, which likely index the degree of cognitive control recruited as well as prediction of outcomes. Notably, RT and error neuron spike rates are internal variables indicative of different processes, as they were uncorrelated (Figures S3A and S3B). We thus next investigated whether iERN amplitude might be correlated with RT using the same multi-level linear model approach (Figure 6C). We found that larger iERN amplitudes were associated with shorter RTs in both dACC and pre-SMA (Figure 6D shows this effect of RT on the iERN amplitude; Figure 6C provides statistics; the significance of this RT effect was evaluated by a likelihood ratio test: for dACC, $\chi^2(1) = 14.61$, $p = 0.0001$; for pre-SMA, $\chi^2(1) = 5.325$, $p = 0.021$). This negative correlation was significant after

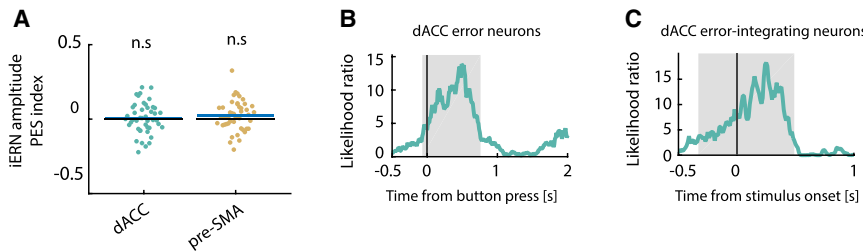


Figure 7. Error Neuron-iERN Synchrony during Errors Predicts Engagement of Control

(A) iERN amplitude did not predict post-error slowing (PES) significantly. Mean values of the PES index (see STAR Methods) for iERN amplitudes were not significantly different from zero. Blue bars denote mean values; black bars denote zero.

(B) The correlation between iERN amplitude and error neuron spike rates (as a function of time; quantified as the likelihood ratio in model com-

parison; see STAR Methods) predicted the extent of post-error slowing (PES) in the dACC. $t = 0$ is button press. The same analysis in the pre-SMA did not yield a statistically significant relationship.

(C) The spike rates of error-integrating neurons in dACC around the time of stimulus onset predicted PES.

* $p \leq 0.05$, ** $p \leq 0.01$, *** $p \leq 0.001$. Error bars represent \pm SEM across cells.

controlling for stimulus congruence, which by itself would have resulted in RT differences (see Figure S4G for RT comparisons for error trials; for dACC, $\chi^2(1) = 9.54$, $p = 0.002$; for pre-SMA, $\chi^2(1) = 4.83$, $p = 0.028$). Thus, the faster an error was made, the larger the iERN amplitude was on that trial. Together, these data revealed two distinct components of the iERN: one that is positively correlated with error neuron spike rate (action outcome information) and one that is negatively correlated with RT, putatively action-outcome prediction error (Alexander and Brown, 2011).

Neural Signatures of PES in dACC

We next sought to determine which aspects of the performance monitoring circuitry interface with the control processes that result in PES. Note that previous efforts to correlate the magnitude of error monitoring signals measured using scalp EEG to PES have yielded contradictory results (Gehring and Fencsik, 2001; Debener et al., 2005; Nieuwenhuis et al., 2001; Hajcak et al., 2003). The evoked potential likely reflects synaptic inputs to a brain region. If so, this synaptic input would then subsequently cause the local responses we measure as spiking activity of neurons in the same region. Given this, we investigate the hypothesis that the ERN itself does not predict PES, but that the ensuing relationship between the ERN and the activity of error neurons does.

We first tested whether the amplitude of the iERN is indicative of PES. Error trials were separated into two groups (for each session): one that leads to PES larger than the median value, and the other that leads to PES smaller than the median value. We then assessed whether the iERN amplitude differed between these two groups (quantified by the “large-small PES” index, zero equals no difference, see STAR Methods). Consistent with some previous EEG studies (Gehring and Fencsik, 2001; Nieuwenhuis et al., 2001; Hajcak et al., 2003), we did not find a significant relationship between iERN amplitude and PES (Figure 7A).

We next investigated whether neural synchrony would predict PES. Here, we assessed neural synchrony by the extent to which spike rates of an error neuron co-vary with the amplitude of the iERN (Nir et al., 2007). This correlation measure could also indicate the efficacy of iERN inputs in driving the local neuronal error signal that is important for control recruitment. We used a multi-level model (see STAR Methods) to assess whether there was a significant interaction between spike rate of error neurons and

the large-small PES categorical variable in predicting iERN amplitude trial by trial. This revealed that in dACC, the stronger the iERN-spike rate correlation around the time an error was committed, the larger was the subsequent PES (Figure 7B; the maximal likelihood ratio is 13.9; $p = 0.015$ obtained by cluster-based permutation test. See STAR Methods for details; the same analysis with type II error neurons in dACC and both types of error neurons in pre-SMA did not yield a statistically significant relationship, see Figures S7D and S7E). Note that while the strength of the correlation between the iERN and error neuron firing rate (in dACC) was thus predictive of PES, both underlying variables themselves were not (“large-small PES” index, $p > 0.5$, $z = 0.46$ for iERN and $p > 0.5$, $z = -0.17$ for spike rate within [0 1]s post button press, signed-rank test; see also Figure 7A).

Error-integrating neurons in dACC signaled whether an error was committed in the previous trial by increasing their spike rates around stimulus onset. This pattern suggests that these neurons could be involved in implementing PES. To investigate this, we tested the relationship between spike rates of error-integrating neurons and PES (see STAR Methods). Spike rates of dACC error-integrating neurons around the time of stimulus onset in post-error trials were significantly predictive of the size of PES (Figure 7C; maximal likelihood ratio is 18.3; $p < 0.001$, cluster-based permutation test; as shown in Figure 3D). This effect also holds if we used the spike counts within the peri-stimulus epoch ([−500 500]ms relative to the stimulus onset; Figure S7F; $p < 0.001$, $\chi^2(1) = 15.76$, likelihood ratio test). We found no significant relationship between their spike rates and the levels of PES for pre-SMA error integrating neurons (Figure S7F; $p = 0.07$, $\chi^2(1) = 3.31$, likelihood ratio test). We thus found two aspects of error monitoring that were predictive of the extent to which control was engaged (all in dACC only): iERN-error neuron spike rate coupling, and spike rates of error-integrating neurons. These two signals occurred at different points in time, suggesting that they are involved in bridging monitoring and corrective control.

DISCUSSION

Here, we provide direct recordings of single neurons in the human MFC that signal errors that are detected endogenously, before external feedback was presented and without the presence of an additional sensory signal to indicate task set (such

as a stop signal). Error neurons were largely distinct from neurons signaling conflict shortly following stimulus onset, arguing that the representation of conflict and error monitoring in MFC are largely distinct. Conflict neurons were also modulated by the state of control: their activity differed between error incongruent and correct incongruent trials. This was not the case for type I error neurons nor for error-integrating neurons, highlighting their putative roles in monitoring and actively mediating control, respectively. It remains an open question whether the error neurons that signal self-monitoring are functionally distinct from neurons that monitor external feedback, reward manipulations, or prediction errors that have been described in detail in macaques (Ito et al., 2003; Stuphorn et al., 2000; Scangos et al., 2013; Matsumoto et al., 2003, 2007; Amiez et al., 2006; Ebitz and Platt, 2015; Hayden et al., 2011).

Despite evidence that the ERN (Gehring et al., 1993; Bonini et al., 2014; Brazdil et al., 2005; Godlove et al., 2011; Emeric et al., 2008; Falkenstein et al., 1991) originates from within dACC and/or pre-SMA (Dehaene et al., 1994; Debener et al., 2005), its relationship with neuronal spiking activity has not been clear. Our report shows that error neuron responses predict the amplitude of the iERN in both of these areas. Further, we showed that the iERNs recorded in pre-SMA (1) occurred earlier, (2) had larger amplitude, (3) were correlated in both amplitude and latency on a trial-by-trial basis with iERNs recorded simultaneously in dACC. These results are consistent with earlier studies (Bonini et al., 2014; Emeric et al., 2010). Our findings argue that both dACC and pre-SMA contribute to the ERN, but at different points in time.

This pattern of findings is consistent with two interpretations. One interpretation is that pre-SMA and dACC both receive inputs carrying error information in parallel, but pre-SMA receives the information earlier than dACC. This scenario is consistent with an influential computational account where synchronized disinhibition of dACC pyramidal cells by dopaminergic projections generates the iERN in dACC (Holroyd and Coles, 2002) and suggest that in pre-SMA similar disinhibition can also occur, but at earlier points of time. But a second possible interpretation is that pre-SMA provides error-related signals as an input to dACC, an interpretation that is consistent with a previous report where error-related evoked potentials in pre-SMA and SMA strictly precede those in the rostral cingulate zone (Bonini et al., 2014). Such a feedforward architecture could interpose additional relays as error signals are communicated indirectly from pre-SMA to dACC, for instance, through the basal ganglia (Nachev et al., 2008; Jahanshahi et al., 2015). Future experiments utilizing causal manipulations will be necessary to probe the role of this putative feedforward connection in error processing.

Strong coupling between LFP components (here measured by the iERN) and spike rates is well documented in sensory cortices, where the coupling is often driven in part by common sensory inputs (but see Kayser et al., 2004). However, in brain areas removed from direct sensory inputs, such as the hippocampus and inferior temporal cortex, these two measures of neural activity diverge and encode information independently (Kreiman et al., 2006; Ekstrom et al., 2007; Ekstrom, 2010). The strong and transient ERN-spike rate coupling in MFC reported we found

is thus notable, because it shows that such phenomenon can occur in brain areas whose primary functions are not sensory information processing. Evoked potentials such as the ERN are thought to reflect spatial summation of large numbers of post-synaptic potentials that synchronize to a substantial degree. Previous work has demonstrated that variation in LFP-spoke rate coupling strength is commensurate with the level of synchronization between two neurons within a local population (Nir et al., 2007) and that the LFP can serve as an index of local information content carried by neurons (Kreiman et al., 2006). The correlation between iERN amplitude and spike rates of error neurons we find here is likely a reflection of the neuronal synchronization that underlies the detection and representation of self-generated errors and/or more effective transmission of error information from other brain structures to the MFC. Notably, this relationship was specific to error neurons and to error trials: we found no significant correlation between similar deflections in the intracranial LFP during correct trials. It is thus likely the case that a separate group of neurons (which we did not describe here) receives the synaptic inputs that are synchronized during correct trials.

PES is one of the most studied consequences of error detection. PES is thought to be jointly produced by two types of cognitive control processes. One type is concerned with sensory information processing, reflected in the up- and downregulation of task-relevant and task-irrelevant sensory areas (Danielmeier et al., 2011; King et al., 2010), as well as adjustments to the parameters of parietal sensory integration processes (Purcell and Kiani, 2016). The second type is concerned with engagement of response inhibition by error monitoring by MFC. BOLD activity within MFC is correlated with activity in task-related visual and motor areas, as well as the size of PES (Danielmeier et al., 2011; Kerns et al., 2004). Inactivation and lesioning of MFC abolishes PES (Narayanan et al., 2013; Kennerley et al., 2006), and individual differences in the white matter integrity of inhibitory networks that include pre-SMA (Aron and Poldrack, 2006; Aron et al., 2007; Jahanshahi et al., 2015) are correlated with the size of PES (Danielmeier et al., 2011). Although these studies unequivocally demonstrate the involvement of MFC in PES, they do not provide insight into how MFC neurons communicate error signals to the control processes that mediate PES. Here, we show that neuronal synchronization may provide a basis for recruiting control by MFC. We find that the strength of the correlation between iERN amplitude and the spike rates of error neurons is predictive of PES in dACC (but not pre-SMA). This suggests that the more synchronized the dACC error neurons are with neighboring neuronal population during errors, the larger the ensuing PES is. Given that neuronal synchronization can potentially represent information with high fidelity (Rutishauser et al., 2010; Wong et al., 2016) and thus have stronger impact on downstream targets (Siegel et al., 2012), our finding suggests that neuronal synchronization may underlie dACC-mediated PES.

Our results suggest that coordinated neural activity can serve as a substrate for information routing that enables the performance-monitoring system to communicate the need for behavioral control to other brain regions, including those that maintain flexible goal information, such as the lateral prefrontal cortex and the frontal polar cortex (Koechlin and Hyafil, 2007; Tsujimoto

et al., 2010; Mansouri et al., 2017; Voytek et al., 2015). The present study offers new insights into the mechanisms of ERN generation and provides potential neural targets for validating the use of the ERN as an endophenotype for psychiatric illness (Olvet and Hajcak, 2008).

STAR★METHODS

Detailed methods are provided in the online version of this paper and include the following:

- KEY RESOURCES TABLE
- CONTACT FOR RESOURCE SHARING
- EXPERIMENTAL MODEL AND SUBJECT DETAILS
 - Depth electrode subjects
 - Scalp EEG subjects
- METHOD DETAILS
 - Task
 - Electrophysiology
 - Electrode localization
 - Spike detection and sorting
- QUANTIFICATION AND STATISTICAL ANALYSIS
 - Behavioral analyses
 - Selection of neurons
 - Single-neuron ROC analysis
 - Temporal profile of neuronal response
 - Single-trial spike train latency
 - Single-trial iERN amplitude and latency extraction
 - Single-trial CP amplitude and latency extraction
 - ROC analysis of iERN amplitude
 - Time-frequency analysis of iEEG signal
 - Multi-level models
 - Scalp EEG – Analysis
 - Waveform analyses
- DATA AND SOFTWARE AVAILABILITY

SUPPLEMENTAL INFORMATION

Supplemental Information includes seven figures and three tables and can be found with this article online at <https://doi.org/10.1016/j.neuron.2018.11.016>.

ACKNOWLEDGMENTS

This work was supported by NIH (P50MH094258, R01MH110831, U01NS103792), an NSF CAREER award (1554105 to U.R.), and the McKnight Endowment for Neuroscience (to U.R.). The funders had no role in study design, data collection, data analysis, decision to publish, or preparation of the manuscript.

AUTHOR CONTRIBUTIONS

Z.F., R.A., and U.R. designed the study. Z.F. and U.R. collected the data. Z.F., R.A., and U.R. analyzed the data and implemented analysis procedures. Z.F., U.R., A.N.M., and R.A. wrote the paper. D.-A.J.W. acquired and analyzed scalp EEG data. J.M.C. provided patient care and facilitated experiments. A.N.M. and I.R. performed surgery.

DECLARATION OF INTERESTS

The authors declare no competing interests.

Received: August 14, 2018
Revised: October 12, 2018
Accepted: November 8, 2018
Published: December 4, 2018

REFERENCES

- Aarts, E., Verhage, M., Veenvliet, J.V., Dolan, C.V., and van der Sluis, S. (2014). A solution to dependency: Using multilevel analysis to accommodate nested data. *Nat. Neurosci.* 17, 491–496.
- Alexander, W.H., and Brown, J.W. (2011). Medial prefrontal cortex as an action-outcome predictor. *Nat. Neurosci.* 14, 1338–1344.
- Amiez, C., Joseph, J.P., and Procyk, E. (2006). Reward encoding in the monkey anterior cingulate cortex. *Cereb. Cortex* 16, 1040–1055.
- Aron, A.R., and Poldrack, R.A. (2006). Cortical and subcortical contributions to Stop signal response inhibition: Role of the subthalamic nucleus. *J. Neurosci.* 26, 2424–2433.
- Aron, A.R., Behrens, T.E., Smith, S., Frank, M.J., and Poldrack, R.A. (2007). Triangulating a cognitive control network using diffusion-weighted magnetic resonance imaging (MRI) and functional MRI. *J. Neurosci.* 27, 3743–3752.
- Barthó, P., Hirase, H., Monconduit, L., Zugaro, M., Harris, K.D., and Buzsáki, G. (2004). Characterization of neocortical principal cells and interneurons by network interactions and extracellular features. *J. Neurophysiol.* 92, 600–608.
- Behrens, T.E., Woolrich, M.W., Walton, M.E., and Rushworth, M.F. (2007). Learning the value of information in an uncertain world. *Nat. Neurosci.* 10, 1214–1221.
- Bonini, F., Burle, B., Liégeois-Chauvel, C., Régis, J., Chauvel, P., and Vidal, F. (2014). Action monitoring and medial frontal cortex: Leading role of supplementary motor area. *Science* 343, 888–891.
- Botvinick, M.M., Braver, T.S., Barch, D.M., Carter, C.S., and Cohen, J.D. (2001). Conflict monitoring and cognitive control. *Psychol. Rev.* 108, 624–652.
- Brainard, D.H. (1997). The Psychophysics Toolbox. *Spat. Vis.* 10, 433–436.
- Brazdil, M., Roman, R., Daniel, P., and Rektor, I. (2005). Intracerebral error-related negativity in a simple Go/NoGo task. *J. Psychophysiol.* 19, 244–255.
- Brown, J.W., and Braver, T.S. (2005). Learned predictions of error likelihood in the anterior cingulate cortex. *Science* 307, 1118–1121.
- Burle, B., Roger, C., Allain, S., Vidal, F., and Hasbroucq, T. (2008). Error negativity does not reflect conflict: A reappraisal of conflict monitoring and anterior cingulate cortex activity. *J. Cogn. Neurosci.* 20, 1637–1655.
- Danielmeier, C., Eichele, T., Forstmann, B.U., Tittgemeyer, M., and Ullsperger, M. (2011). Posterior medial frontal cortex activity predicts post-error adaptations in task-related visual and motor areas. *J. Neurosci.* 31, 1780–1789.
- Debener, S., Ullsperger, M., Siegel, M., Fiehler, K., von Cramon, D.Y., and Engel, A.K. (2005). Trial-by-trial coupling of concurrent electroencephalogram and functional magnetic resonance imaging identifies the dynamics of performance monitoring. *J. Neurosci.* 25, 11730–11737.
- Dehaene, S., Posner, M.I., and Tucker, D.M. (1994). Localization of a neural system for error-detection and compensation. *Psychol. Sci.* 5, 303–305.
- Dutilh, G., van Ravenzwaaij, D., Nieuwenhuis, S., van der Maas, H.L.J., Forstmann, B.U., and Wagenmakers, E.J. (2012). How to measure post-error slowing: A confound and a simple solution. *J. Math. Psychol.* 56, 208–216.
- Ebitz, R.B., and Platt, M.L. (2015). Neuronal activity in primate dorsal anterior cingulate cortex signals task conflict and predicts adjustments in pupil-linked arousal. *Neuron* 85, 628–640.
- Ekstrom, A. (2010). How and when the fMRI BOLD signal relates to underlying neural activity: The danger in dissociation. *Brain Res. Brain Res. Rev.* 62, 233–244.
- Ekstrom, A., Viskontas, I., Kahana, M., Jacobs, J., Upchurch, K., Bookheimer, S., and Fried, I. (2007). Contrasting roles of neural firing rate and local field potentials in human memory. *Hippocampus* 17, 606–617.
- Emeric, E.E., Brown, J.W., Leslie, M., Pouget, P., Stuphorn, V., and Schall, J.D. (2008). Performance monitoring local field potentials in the medial frontal cortex of primates: Anterior cingulate cortex. *J. Neurophysiol.* 99, 759–772.

- Emeric, E.E., Leslie, M., Pouget, P., and Schall, J.D. (2010). Performance monitoring local field potentials in the medial frontal cortex of primates: Supplementary eye field. *J. Neurophysiol.* 104, 1523–1537.
- Falkenstein, M., Hohnsbein, J., Hoormann, J., and Blanke, L. (1991). Effects of crossmodal divided attention on late ERP components. II. Error processing in choice reaction tasks. *Electroencephalogr. Clin. Neurophysiol.* 78, 447–455.
- Frank, M.J., Woroch, B.S., and Curran, T. (2005). Error-related negativity predicts reinforcement learning and conflict biases. *Neuron* 47, 495–501.
- Gehring, W.J., and Fencsik, D.E. (2001). Functions of the medial frontal cortex in the processing of conflict and errors. *J. Neurosci.* 21, 9430–9437.
- Gehring, W.J., Goss, B., Coles, M.G.H., Meyer, D.E., and Donchin, E. (1993). A neural system for error-detection and compensation. *Psychol. Sci.* 4, 385–390.
- Gerbrandt, L.K., Lawrence, J.C., Eckardt, M.J., and Lloyd, R.L. (1978). Origin of the neocortically monitored theta rhythm in the curarized rat. *Electroencephalogr. Clin. Neurophysiol.* 45, 454–467.
- Godlove, D.C., Emery, E.E., Segovis, C.M., Young, M.S., Schall, J.D., and Woodman, G.F. (2011). Event-related potentials elicited by errors during the stop-signal task. I. Macaque monkeys. *J. Neurosci.* 31, 15640–15649.
- Hajcak, G., McDonald, N., and Simons, R.F. (2003). To err is autonomic: Error-related brain potentials, ANS activity, and post-error compensatory behavior. *Psychophysiology* 40, 895–903.
- Hanes, D.P., Thompson, K.G., and Schall, J.D. (1995). Relationship of presaccadic activity in frontal eye field and supplementary eye field to saccade initiation in macaque: Poisson spike train analysis. *Exp. Brain Res.* 103, 85–96.
- Harris, K.D., Henze, D.A., Csicsvari, J., Hirase, H., and Buzsáki, G. (2000). Accuracy of tetrode spike separation as determined by simultaneous intracellular and extracellular measurements. *J. Neurophysiol.* 84, 401–414.
- Hayden, B.Y., Heilbronner, S.R., Pearson, J.M., and Platt, M.L. (2011). Surprise signals in anterior cingulate cortex: Neuronal encoding of unsigned reward prediction errors driving adjustment in behavior. *J. Neurosci.* 31, 4178–4187.
- Holroyd, C.B., and Coles, M.G.H. (2002). The neural basis of human error processing: Reinforcement learning, dopamine, and the error-related negativity. *Psychol. Rev.* 109, 679–709.
- Isoda, M., and Hikosaka, O. (2007). Switching from automatic to controlled action by monkey medial frontal cortex. *Nat. Neurosci.* 10, 240–248.
- Ito, S., Stuphorn, V., Brown, J.W., and Schall, J.D. (2003). Performance monitoring by the anterior cingulate cortex during saccade countermanding. *Science* 302, 120–122.
- Jahanshahi, M., Obeso, J., Rothwell, J.C., and Obeso, J.A. (2015). A fronto-striato-subthalamic-pallidal network for goal-directed and habitual inhibition. *Nat. Rev. Neurosci.* 16, 719–732.
- Kayser, C., Kim, M., Ugurbil, K., Kim, D.S., and König, P. (2004). A comparison of hemodynamic and neural responses in cat visual cortex using complex stimuli. *Cereb. Cortex* 14, 881–891.
- Kennerley, S.W., Walton, M.E., Behrens, T.E., Buckley, M.J., and Rushworth, M.F. (2006). Optimal decision making and the anterior cingulate cortex. *Nat. Neurosci.* 9, 940–947.
- Kerns, J.G., Cohen, J.D., MacDonald, A.W., 3rd, Cho, R.Y., Stenger, V.A., and Carter, C.S. (2004). Anterior cingulate conflict monitoring and adjustments in control. *Science* 303, 1023–1026.
- King, J.A., Korb, F.M., von Cramon, D.Y., and Ullsperger, M. (2010). Post-error behavioral adjustments are facilitated by activation and suppression of task-relevant and task-irrelevant information processing. *J. Neurosci.* 30, 12759–12769.
- Koechlin, E., and Hyafil, A. (2007). Anterior prefrontal function and the limits of human decision-making. *Science* 318, 594–598.
- Kolling, N., Wittmann, M.K., Behrens, T.E., Boorman, E.D., Mars, R.B., and Rushworth, M.F. (2016). Value, search, persistence and model updating in anterior cingulate cortex. *Nat. Neurosci.* 19, 1280–1285.
- Kreiman, G., Hung, C.P., Kraskov, A., Quiroga, R.Q., Poggio, T., and DiCarlo, J.J. (2006). Object selectivity of local field potentials and spikes in the macaque inferior temporal cortex. *Neuron* 49, 433–445.
- Laming, D. (1979). Choice Reaction Performance Following an Error. *Acta Psychol. (Amst.)* 43, 199–224.
- Logothetis, N.K., Kayser, C., and Oeltermann, A. (2007). In vivo measurement of cortical impedance spectrum in monkeys: Implications for signal propagation. *Neuron* 55, 809–823.
- Luck, S.J. (2014). A closer look at ERPs and ERP components. In *An Introduction to the Event-Related Potential Technique*, Second Edition, S.J. Luck, ed. (MIT Press).
- Luu, P., Tucker, D.M., and Makeig, S. (2004). Frontal midline theta and the error-related negativity: Neurophysiological mechanisms of action regulation. *Clin. Neurophysiol.* 115, 1821–1835.
- Mansouri, F.A., Koechlin, E., Rosa, M.G.P., and Buckley, M.J. (2017). Managing competing goals—A key role for the frontopolar cortex. *Nat. Rev. Neurosci.* 18, 645–657.
- Maris, E., and Oostenveld, R. (2007). Nonparametric statistical testing of EEG- and MEG-data. *J. Neurosci. Methods* 164, 177–190.
- Matsumoto, K., Suzuki, W., and Tanaka, K. (2003). Neuronal correlates of goal-based motor selection in the prefrontal cortex. *Science* 301, 229–232.
- Matsumoto, M., Matsumoto, K., Abe, H., and Tanaka, K. (2007). Medial prefrontal cell activity signaling prediction errors of action values. *Nat. Neurosci.* 10, 647–656.
- Minxha, J., Mosher, C., Morrow, J.K., Mamelak, A.N., Adolphs, R., Gothard, K.M., and Rutishauser, U. (2017). Fixations gate species[HYPHEN]specific responses to free viewing of faces in the human and macaque amygdala. *Cell Reports* 18, 878–891.
- Mitchell, J.F., Sundberg, K.A., and Reynolds, J.H. (2007). Differential attention-dependent response modulation across cell classes in macaque visual area V4. *Neuron* 55, 131–141.
- Nachev, P., Kennard, C., and Husain, M. (2008). Functional role of the supplementary and pre-supplementary motor areas. *Nat. Rev. Neurosci.* 9, 856–869.
- Narayanan, N.S., Cavanagh, J.F., Frank, M.J., and Laubach, M. (2013). Common medial frontal mechanisms of adaptive control in humans and rodents. *Nat. Neurosci.* 16, 1888–1895.
- Niessing, J., Ebisch, B., Schmidt, K.E., Niessing, M., Singer, W., and Galuske, R.A. (2005). Hemodynamic signals correlate tightly with synchronized gamma oscillations. *Science* 309, 948–951.
- Nieuwenhuis, S., Ridderinkhof, K.R., Blom, J., Band, G.P., and Kok, A. (2001). Error-related brain potentials are differentially related to awareness of response errors: Evidence from an antisaccade task. *Psychophysiology* 38, 752–760.
- Nir, Y., Fisch, L., Mukamel, R., Gelbard-Sagiv, H., Arieli, A., Fried, I., and Malach, R. (2007). Coupling between neuronal firing rate, gamma LFP, and BOLD fMRI is related to interneuronal correlations. *Curr. Biol.* 17, 1275–1285.
- Olvet, D.M., and Hajcak, G. (2008). The error-related negativity (ERN) and psychopathology: Toward an endophenotype. *Clin. Psychol. Rev.* 28, 1343–1354.
- Olvet, D.M., and Hajcak, G. (2009). The stability of error-related brain activity with increasing trials. *Psychophysiology* 46, 957–961.
- Pesaran, B., Vinck, M., Einevoll, G.T., Sirota, A., Fries, P., Siegel, M., Truccolo, W., Schroeder, C.E., and Srinivasan, R. (2018). Investigating large-scale brain dynamics using field potential recordings: Analysis and interpretation. *Nat. Neurosci.* 21, 903–919.
- Pouzat, C., Mazor, O., and Laurent, G. (2002). Using noise signature to optimize spike-sorting and to assess neuronal classification quality. *J. Neurosci. Methods* 122, 43–57.
- Purcell, B.A., and Kiani, R. (2016). Neural mechanisms of post-error adjustments of decision policy in parietal cortex. *Neuron* 89, 658–671.
- Quilodran, R., Rothé, M., and Procyk, E. (2008). Behavioral shifts and action valuation in the anterior cingulate cortex. *Neuron* 57, 314–325.

- Rabbitt, P.M.A. (1966). Error correction time without external error signals. *Nature* **212**, 438.
- Ridderinkhof, K.R., Ullsperger, M., Crone, E.A., and Nieuwenhuis, S. (2004). The role of the medial frontal cortex in cognitive control. *Science* **306**, 443–447.
- Rushworth, M.F., and Behrens, T.E. (2008). Choice, uncertainty and value in prefrontal and cingulate cortex. *Nat. Neurosci.* **11**, 389–397.
- Rutishauser, U., Schuman, E.M., and Mamelak, A.N. (2006). Online detection and sorting of extracellularly recorded action potentials in human medial temporal lobe recordings, *in vivo*. *J. Neurosci. Methods* **154**, 204–224.
- Rutishauser, U., Ross, I.B., Mamelak, A.N., and Schuman, E.M. (2010). Human memory strength is predicted by theta-frequency phase-locking of single neurons. *Nature* **464**, 903–907.
- Rutishauser, U., Ye, S., Koroma, M., Tudusciuc, O., Ross, I.B., Chung, J.M., and Mamelak, A.N. (2015). Representation of retrieval confidence by single neurons in the human medial temporal lobe. *Nat. Neurosci.* **18**, 1041–1050.
- Scangos, K.W., Aronberg, R., and Stuphorn, V. (2013). Performance monitoring by presupplementary and supplementary motor area during an arm movement countermanding task. *J. Neurophysiol.* **109**, 1928–1939.
- Schmitzer-Torbert, N., Jackson, J., Henze, D., Harris, K., and Redish, A.D. (2005). Quantitative measures of cluster quality for use in extracellular recordings. *Neuroscience* **131**, 1–11.
- Shenhav, A., Botvinick, M.M., and Cohen, J.D. (2013). The expected value of control: An integrative theory of anterior cingulate cortex function. *Neuron* **79**, 217–240.
- Sheth, S.A., Mian, M.K., Patel, S.R., Asaad, W.F., Williams, Z.M., Dougherty, D.D., Bush, G., and Eskandar, E.N. (2012). Human dorsal anterior cingulate cortex neurons mediate ongoing behavioural adaptation. *Nature* **488**, 218–221.
- Shima, K., and Tanji, J. (1998). Role for cingulate motor area cells in voluntary movement selection based on reward. *Science* **282**, 1335–1338.
- Siegel, M., Donner, T.H., and Engel, A.K. (2012). Spectral fingerprints of large-scale neuronal interactions. *Nat. Rev. Neurosci.* **13**, 121–134.
- Sirota, A., Montgomery, S., Fujisawa, S., Isomura, Y., Zugaro, M., and Buzsáki, G. (2008). Entrainment of neocortical neurons and gamma oscillations by the hippocampal theta rhythm. *Neuron* **60**, 683–697.
- Stuphorn, V., and Schall, J.D. (2006). Executive control of countermanding saccades by the supplementary eye field. *Nat. Neurosci.* **9**, 925–931.
- Stuphorn, V., Taylor, T.L., and Schall, J.D. (2000). Performance monitoring by the supplementary eye field. *Nature* **408**, 857–860.
- Tadel, F., Bailet, S., Mosher, J.C., Pantazis, D., and Leahy, R.M. (2011). Brainstorm: A user-friendly application for MEG/EEG analysis. *Comput. Intell. Neurosci.* **2011**, 879716.
- Trujillo, L.T., and Allen, J.J. (2007). Theta EEG dynamics of the error-related negativity. *Clin. Neurophysiol.* **118**, 645–668.
- Tsujimoto, S., Genovesio, A., and Wise, S.P. (2010). Evaluating self-generated decisions in frontal pole cortex of monkeys. *Nat. Neurosci.* **13**, 120–126.
- Ullsperger, M., and Danielmeier, C. (2016). Reducing speed and sight: How adaptive is post-error slowing? *Neuron* **89**, 430–432.
- Ullsperger, M., Danielmeier, C., and Jocham, G. (2014). Neurophysiology of performance monitoring and adaptive behavior. *Physiol. Rev.* **94**, 35–79.
- Vogt, B.A., Berger, G.R., and Derbyshire, S.W. (2003). Structural and functional dichotomy of human midcingulate cortex. *Eur. J. Neurosci.* **18**, 3134–3144.
- Voytek, B., Kayser, A.S., Badre, D., Fegen, D., Chang, E.F., Crone, N.E., Parvizi, J., Knight, R.T., and D'Esposito, M. (2015). Oscillatory dynamics coordinating human frontal networks in support of goal maintenance. *Nat. Neurosci.* **18**, 1318–1324.
- Wang, C., Ulbert, I., Schomer, D.L., Marinkovic, K., and Halgren, E. (2005). Responses of human anterior cingulate cortex microdomains to error detection, conflict monitoring, stimulus-response mapping, familiarity, and orienting. *J. Neurosci.* **25**, 604–613.
- Williams, Z.M., Bush, G., Rauch, S.L., Cosgrove, G.R., and Eskandar, E.N. (2004). Human anterior cingulate neurons and the integration of monetary reward with motor responses. *Nat. Neurosci.* **7**, 1370–1375.
- Winter, B. (2013). Linear models and linear mixed effects models in R with linguistic applications. arXiv, arXiv:1308.5499 <https://arxiv.org/abs/1308.5499>.
- Wong, Y.T., Fabiszak, M.M., Novikov, Y., Daw, N.D., and Pesaran, B. (2016). Coherent neuronal ensembles are rapidly recruited when making a look-reach decision. *Nat. Neurosci.* **19**, 327–334.
- Yeung, N., Bogacz, R., Holroyd, C.B., Nieuwenhuis, S., and Cohen, J.D. (2007). Theta phase resetting and the error-related negativity. *Psychophysiology* **44**, 39–49.

STAR★METHODS**KEY RESOURCES TABLE**

REAGENT or RESOURCE	SOURCE	IDENTIFIER
Software and Algorithms		
MATLAB R2016a	MathWorks	RRID: SCR_001622 https://www.mathworks.com
OSort		RRID: SCR_015869 http://www.rutishauserlab.org/osort
Psychophysics toolbox PTB3		RRID: SCR_002881 http://psychtoolbox.org
Brainstorm 3		RRID:SCR_001761
Other		
Neuralynx Neurophysiology System	Neuralynx Inc	Cat# ATLAS 128
Cedrus Response Box	Cedrus Inc	Cat# RB-740

CONTACT FOR RESOURCE SHARING

Further information and requests for resources should be directed to the Lead Contact, Ueli Rutishauser (rutishauser@csmc.edu).

EXPERIMENTAL MODEL AND SUBJECT DETAILS**Depth electrode subjects**

29 patients (see [Table S1](#) for age and gender) who were evaluated for possible surgical treatment of epilepsy using implantation of depth electrodes volunteered for the study and gave written informed consent. We only included patients with well-isolated single-neuron activity on at least one electrode in the areas of interest.

Scalp EEG subjects

12 naive non-surgical control subjects participated (seven females). All participants gave informed consent, and the protocol was approved by the Caltech Institutional Review Board. A BioSemi Active2 system collected EEG data and laptop event triggers at 1024 Hz. Electrode montages were in Biosemi's standard 64 or 128 channel cap arrays, with additional electrodes for right eye vertical EOG.

METHOD DETAILS**Task**

Subjects performed a speeded version of the classical color-word Stroop task. In each trial, the stimulus was chosen randomly to be one of the three words (red, green and blue) printed in either red, green, or blue color (see [Figure 1A](#)). Subjects were instructed to indicate the color the word was printed in as quickly as possible (ignoring the meaning of the word) by pressing one of the three buttons on an external response box (RB-740, Cedrus Corp., San Pedro, CA). The stimulus was replaced with a blank screen immediately after the button press. One second after button press, subjects were given one of three types of feedback: correct, incorrect, or "too slow." An adaptive staircase procedure was used to establish an RT threshold such that 10%–15% of trials were rated as "too slow" regardless of the accuracy of the response. Correct trials with 'too slow' feedback were not considered as error trials. This dynamic threshold was implemented to encourage faster responses. The inter-trial interval varied randomly from 1–1.5 s. The task was administered in blocks of 90 trials, 30%–40% of which were incongruent (randomly intermixed). Patients performed 3–6 blocks in a session. Trials with RT larger than three standard deviations above the mean were excluded for all analyses. The task was implemented using the Psychophysics Toolbox ([Brainard, 1997](#)). Scalp EEG participants performed the same task as described above (350 trials total).

Electrophysiology

We recorded from up to 4 electrodes in each subject (bilateral dACC and pre-SMA), each with eight high-impedance microwires at the medial end and eight low-impedance macro-contacts along the shaft ([Figure S1A](#); AdTech Medical Inc.). Here, we used only the most medial macro contact (which is located within the dACC or the pre-SMA) and all microwires. We recorded the broadband 0.1Hz–9kHz continuous extracellular signal with a sampling rate of 32–40kHz from each microwire and with a sampling rate of 2kHz from each macro-contact (ATLAS, Neuralynx Inc., Bozeman, MT). One microwire on each electrode served as a local reference (bi-polar recording).

Electrode localization

For each patient, two structural MRI scans were obtained: one before and one after implantation. Electrodes were localized based on these scans in each individual patient. Only electrodes that could be clearly localized to the dACC (cingulate gyrus or cingulate sulcus; for patients with a paracingulate sulcus, electrodes were assigned to the dACC if they were within the paracingulate sulcus or superior cingulate gyrus or the pre-SMA (superior frontal gyrus) were included. We also merged the subject-specific MRI onto an Atlas brain, which was used only for visualization purposes (all localization was based on individual MRIs without using an Atlas). We described the analysis pipeline for transforming the post-implantation MRI into the same space as a MNI152-based atlas previously (Minxha et al., 2017).

Spike detection and sorting

We filtered the raw signal with a zero-phase lag filter in the 300–3000Hz band. Spikes were detected and sorted using a template-matching algorithm (Rutishauser et al., 2006). We carefully evaluated isolation quality of units and analyzed only well-isolated single units. We used the following criteria (see Figures S1D–S1I): i) percentage of ISIs smaller than 3ms, ii) SNR of the waveform, calculated as the ratio of the peak amplitude of the mean waveform of each cluster and the standard deviation of the noise, iii) the pairwise projection distance as provided by the projection test (Pouzat et al., 2002) between all pairs of neurons isolated on the same wire, iv) the modified coefficient of variation of variability in the ISI (CV2), and v) the isolation distance (Schmitzer-Torbert et al., 2005; Harris et al., 2000), which we computed as previously defined (Rutishauser et al., 2006). Channels with inter-ictal epileptic events were excluded. All research protocols were approved by the institutional review boards of Cedars-Sinai Medical Center, Huntington Memorial Hospital and the California Institute of Technology.

QUANTIFICATION AND STATISTICAL ANALYSIS

Behavioral analyses

We constructed a mixed-effect one-way ANOVA model with a nested design to test for the Stroop effect. We entered RT as the response variable, the stimulus type ('congruent' or 'incongruent') as the fixed effect and session number nested within subject ID as a random effect. To test for PES effects, we used two complementary approaches. First, we constructed a mixed-effect one-way ANOVA model with a nested design, with RT as the response variable, the previous outcome and current trial stimulus type ('congruent' or 'incongruent') as the fixed effects and the session numbers nested within subject ID as the random effect. For this model, we also included an interaction term between the two fixed effects. Second, we identified quadruplets of trials that formed a 'CCEC' sequence ('C', correct trial, 'E', error trial) and the stimulus types (congruent or incongruent) were matched for the second and fourth trial within this sequence. This ensured that the PES measure was not confounded by the Stroop effect. For each quadruplet, we then defined the trial-by-trial PES as the difference in RT between the fourth and the second trial in this sequence. We then compared the mean of the trial-by-trial PES extracted this way with zero using a t test to confirm the statistical significance of PES. This PES measure was used for subsequent iERN amplitude-error neuron spike rates correlation analyses and spike-field coherence analyses. This method restricted the post-correct trials to a subset that directly precede the post-error trials to avoid confounding factors due to non-specific RT slowing, a caveat previously described (Dutilh et al., 2012).

Selection of neurons

We only considered neurons that had a mean spike rate > 0.5 Hz. We sought neurons whose spike rate differed significantly between trial types of interest in two epochs that were defined with respect to stimulus onset or action onset (button press): (i) neurons signaling errors ('error neurons'), (ii) neurons signaling preceding trial accuracy ('error-integrating neurons'), (iii) neurons signaling conflicts ('conflict neurons'). We fit a generalized linear model (GLM) to each neuron (using MATLAB function "fitglm.m") and then evaluated whether the model explained significant variance to determine whether a neuron was selective or not for a variable of interest. We entered the spike count in the epoch of interest as the response variable. We entered two predictor variables: i) a dummy variable coding for either trial outcome or previous trial outcome, and, ii) RT (to control for RT effect). A neuron was significantly selective for the outcome predictor variable if the p value for the first predictor was below 0.05 (p value as returned from the fitglm function). The epoch of interest for the error neurons was a 1 s epoch starting immediately after button press ('post-action epoch' or 'postBP epoch', see Figure S2A), comparing between error and correct trials. Only sessions with at least 7 error trials were considered for selecting error neurons, a minimum number of errors that has been demonstrated to be sufficient for stable error signals (Olvet and Hajcak, 2009). The epoch of interest for error-integrating neurons was –0.5 to 0.5 s (1 s length) centered on stimulus onset ('peri-stimulus epoch', see Figure S2A), comparing between EC and CC trials. The epoch of interest for conflict neurons was 0 to 0.5 s after stimulus onset ('post-stimulus epoch', see Figure S2A), comparing between correct congruent and correct incongruent trials.

Each group of neurons was further divided into two sub-categories according to the sign of the spike rate difference (the sign of the regression coefficient of the outcome variable predictor; Type I and II, respectively; Figure S2B). To estimate chance levels of this selection procedure, we repeated the selection procedure (two-tailed bootstrap) 1000 times after randomly permuting the labels to estimate a null distribution (see Figure 3A; for conflict neurons, see Figure S3E). We only analyzed groups of neurons with a size larger than expected by chance ($p < 0.05$).

Single-neuron and group-averaged post-stimulus time histograms (PSTHs) were constructed using non-overlapping bins of 200ms width. PSTH plots were not smoothed and data points were plotted with respect to the center of the bin. Before averaging across neurons, spike rates for each neuron were standardized by subtracting the mean and dividing with the standard deviation of the baseline (-0.7 to -0.2 s relative to the stimulus onset).

Single-neuron ROC analysis

For each neuron, a receiver-operating characteristic (ROC) curve was constructed based on the spike rate in the time windows of interest. The ROC was parametrized by a threshold that varied from the lowest to the highest spike rates in 25 linearly-spaced steps. For each threshold, trials were classified as ‘label 1’ or ‘label 2’ according to whether the spike rate in a given trial was higher or lower than this threshold. True positive rates (‘TPR’) and false positive rates (‘FPR’) were then derived by comparing the assigned labels with the true labels for each threshold. The area under the curve (AUC) of the ROC was used as a summary metric. In order to aggregate AUCs from different neurons, we always assigned the trial type with higher spike rates in the ROI to ‘label 1’. We estimated the AUC values expected by chance by a permutation test.

For the error neurons (Both Type I and Type II, [Figure 3F](#)), we computed AUC values using error- and correct-trial spike rates in the post-action epoch (0-1 s relative to button press). For the error-integrating neurons, we computed AUC values for the spike rates estimated from the following three epochs: (i) 0-1 s relative to feedback onset (error versus correct) in the preceding trials, (ii) -0.5 - 0.5 s relative to stimulus onset (‘peri-stimulus epoch’) in the current trials (EC versus CC) and (iii) 0-1 s after button press in the current trials (‘postBP epoch’; error versus correct).

Temporal profile of neuronal response

We used a sliding-window GLM to quantify the temporal profile of information conveyed by neuronal spike rates of a single neuron about trial outcome (error versus correct; [Figure 4A](#)). We first used a ± 200 ms bin moved across the spike train on each trial in successive 10ms steps. For each of these bins, we entered the spike count as the response variable and the trial outcome (error or correct) as one predictor variable, and RT as another predictor variable. This is because spike rates of the neurons in both dACC and pre-SMA can carry a component that covariates with RT and the effect of trial outcome on spike rates can be isolated after regressing out the RT effect in this principled way. For each bin-wise GLM model, the effect of the trial outcome was quantified by a likelihood ratio, derived from a likelihood ratio test comparing the full model with null model (full model minus the trial outcome predictor). We used the time course of the likelihood ratio to estimate for each neuron the point of time at which it first differentiated between trial outcomes (error versus correct; [Figure 4B](#)). These differential latencies were determined as the first point of time at which the effect size was significant by the likelihood ratio test ($p < 0.05$) for a consecutive 15 time steps (i.e 150 ms).

We used a cross-validated partial correlation analyses to determine the time window (post-action versus post-feedback) in which a population of neurons conveyed the most information about error ([Figure 3G](#)). Here, a Spearman’s partial correlation coefficient was computed by correlating the spike rates of error neurons in the postBP epoch, and the trial outcome dummy variable (error coded as 1, correct coded as 0), while controlling for RT on the same trial. Statistical comparisons between group averages of partial correlation coefficients in different time windows were made using Wilcoxon’s rank sum test. However, the group averages in the same time window used to previously select neurons is biased toward larger values. Here, we circumvented this problem by using cross validation to assure that the group averages were computed from out-of-sample data not used for selection. For this, we performed 200 runs of cross validation. In each run, we randomly subsampled 80% trials for selecting neurons and used the remaining 20% of trials to compute the partial correlation coefficients between spike rates and the relevant trial variable (levels of stimulus congruence or outcomes).

Single-trial spike train latency

We estimated the onset latency in individual trials using Poisson spike-train analysis ([Figure 4C](#)). This method detects points of time at which the observed inter-spike intervals (ISI) deviate significantly from that assumed by a constant-rate Poisson process. This is achieved by maximizing a Poisson surprise index ([Hanes et al., 1995](#)). We used the average spike rate of each neuron as the baseline rate of the underlying Poisson process. Since the error signal is related to action completion, we required that the detected bursts of spikes ended after the action was completed to exclude activation unrelated to button press. We included spikes in a window 300-2000ms after stimulus onset. The statistical threshold for detecting an onset was $p < 0.01$. Repeating the same procedure with a threshold of $p < 0.001$ did not affect our conclusions.

Single-trial iERN amplitude and latency extraction

We determined the amplitude and latency of the iERN on individual trials using the following algorithm. First, for each electrode we determined the peak position of the average iERN waveform within a time window of [-50 200]ms relative to button press. We then defined a time window of 200ms centered on the peak of the average iERN as the region of interest for single-trial estimation. For each trial, we used ‘findpeak’ (MATLAB) to identify all local negative peaks within this time window and then picked the local peak closest to the peak position of the averaged iERN. This approach determines the contribution of each single trial to the average iERN. Since the timing of the iERN is well understood and known (from the average), the negative peak closest in time has the highest likelihood of being the true single-trial iERN signal. The point of time (relative to button press) and voltage value of this *negative-going* peak was

then used as the single-trial iERN latency and amplitude. In [Figure 7A](#), we assessed whether iERN amplitudes differed between PES levels using a PES modulation index computed from the iERN amplitudes. For this, we first separate the error trials into two groups: one that leads to PES values larger than the median value, and one that leads to PES values smaller than the median value (of this experimental session). We then compute the mean iERN amplitude across these two groups of error trials separately. The PES modulation index is equal to the difference of these two mean values divided by their sum.

Single-trial CP amplitude and latency extraction

We determined the amplitude and latency of the CP on individual trials using the following algorithm. First, for each electrode we determined the peak position of the average iERN waveform within a time window of [-50 200]ms relative to button press. We then defined a time window of 200ms centered on this average CP peak position as the region of interest for single-trial estimation. For each trial, we used ‘findpeak’ (MATLAB) to identify all local positive peaks within this time window and then picked the local peak closest to the peak position of the averaged CP. The point of time and voltage value of this *positive-going* peak was then used as the single-trial CP latency and amplitude.

ROC analysis of iERN amplitude

For each electrode, a receiver-operating characteristic (ROC) curve was constructed based on the voltage values extracted by the iERN extraction algorithm (see above) on error and correct trials (but not CP values that are extracted by a different algorithm). The ROC was parametrized by a threshold that varied from the lowest to the highest voltage values in 25 linearly-spaced steps. For each threshold, trials were classified as ‘label 1’ or ‘label 2’ according to whether the voltage value on a given trial was higher or lower than this threshold. True positive rates (‘TPR’) and false positive rates (‘FPR’) were then derived by comparing the assigned labels with the true labels for each threshold. The area under the curve (AUC) of the ROC was used as a summary metric and characterized how well the iERN amplitude on a given trial is indicative of whether the response was correct or incorrect.

Time-frequency analysis of iEEG signal

We used the Hilbert transform to generate time-frequency representations of the iEEG signal. The continuous raw signal (for the entire task) was first down-sampled from 2kHz to 500Hz and then filtered with fourth-order Butterworth filters centered at 28 linearly-spaced frequencies between 1.2 to 11.7Hz. We used ‘filtfilt.m’ (MATLAB) to ensure zero-phase distortion and then Hilbert-transformed the filtered data to obtain the corresponding instantaneous amplitude and phase values. Next, we segmented this signal into epochs with respect to time of stimulus onset or button-press separately. Epochs with raw voltage amplitudes larger than 150uV were excluded (< 1% of trials were excluded). Power estimates for each frequency bins were generated by squaring the corresponding instantaneous amplitude, averaged across trials and then combined to form a time-frequency representation. For this, we equalized the trial number and RT across conditions. For normalization, time-frequency spectrograms were divided by the corresponding baseline power for each frequency band and log-transformed into decibels (dB). Baseline power was estimated by averaging across all trials in the pre-stimulus epoch (-0.7 s to -0.2 s relative to stimulus onset). To test for a correlation between iERN amplitude and theta-band power, we computed the Spearman’s rank correlation coefficient for each session and tested the mean of correlation coefficients versus zero. To analyze induced power, we repeated above analyses after subtracting event-related potentials. For this, we first computed the event-related potentials and then subtracted these from each trial for each condition (error and correct trials) separately.

Multi-level models

We constructed linear multi-level models ([Aarts et al., 2014](#); [Winter, 2013](#)) to test for relationships between RT, iERN amplitude, and error neuron spike rates. For all of the following analyses, we used only data from error trials. For [Figure 6A](#), in the bin-wise model we entered iERN amplitude as the response variable, spike counts in each ± 300 ms bin (the center of the bin moved from -0.5 s to 2 s relative to button press in steps of 10ms) and RT as the fixed effects, session number as the random intercept and cell number nested within subject ID as the random slope for the effect of spike counts. For [Figure 6C](#), we entered iERN amplitude as the response variable, RT as the fixed effect, session number as the random intercept and session number nested within subject ID as the random slope for the effect of RT. For [Figure 7B](#), the model setup is the same as that in [Figure 6A](#) except that we added a dummy variable (‘PES levels’) indicating whether an error trial corresponds to larger (assigned “1”) or smaller (assigned “0”) PES than the median PES (of the session) and estimated it as the main effect and its interaction with the spike counts. For [Figure 7C](#), the bin-wise model has the spike rates of error-integrating neurons within each ± 300 ms bin as the response variable, the PES level and RT as the fixed effects and session number nested within subject ID as the random slope for the effect of RT. For [Figure S7D](#), the spike counts of error neurons used in the models were all within the postBP epoch ([0 1]s after button press). The statistical significance of all the models described above was evaluated by a model comparison approach ([Winter, 2013](#)). Using the likelihood ratio test, we derived the likelihood ratio by comparing the full model and a null model (obtained from the full model by removing the effect of interest, leaving all the other fixed or random effects unchanged). The log likelihood ratio distributes asymptotically as a chi-square distribution and a theoretical p value can thus be computed. For [Figures 6A, 7B, and 7C](#), we performed cluster-based permutation test to control for multiple comparison ([Maris and Oostenveld, 2007](#)). To generate an empirical null distribution (1000 permutations) of likelihood ratio for each bin, we permuted the iERN amplitude data so that each iERN amplitude no longer matched with the spike rate data, while

keeping the rest of the model unchanged. We then derived the likelihood ratio using the permuted data by the same model comparison approach. During each iteration, we thresholded the likelihood ratio at the value of 3.84 to identify connected clusters, and then computed the sum of likelihood ratio from each cluster and took the maximum of these sums as the test statistic. The true statistic for the cluster (computed using original un-permuted data) was finally compared with the empirical null distribution to derive a p value.

Scalp EEG – Analysis

Data were analyzed using Brainstorm 3 ([Tadel et al., 2011](#)). Data was re-referenced to average, and then band-pass filtered between 1–16 Hz. Eye-blanks were automatically marked and artifacts removed via peak detection in the VEOG and signal space projection algorithms. Button-press events were added to the EEG record based on the stimulus onset triggers and precise RTs recorded by the response box (RB-740, Cedrus Inc.). Trial epochs were baseline corrected by the mean potential from −0.7 s to −0.2 s relative to button-press. To balance correct and error trials in number and RT, each subject's correct trials were subsampled by selecting the trials with the RTs most closely matching each error trials' RTs. ERPs were calculated for each subjects' error trials (ERN) and correct trials (CRN). ERN statistics were calculated by taking each subjects' ERP peak negativity between −50ms to 200ms relative to the button press. ERN and CRN peaks were compared across subjects by paired t test. The control subjects demonstrated a robust Stroop effect (65.2 ± 0.9 ms, mean ± s.e.m. across sessions, $F(1,11) = 54.07$, $p < 10^{-10}$, mixed-effect one-way ANOVA with random effect) and PES (69.0 ± 22.3 ms, mean ± s.e.m. across sessions, $F(1,32) = 7.3$, $p = 0.01$) and made errors in $14.8 \pm 1.3\%$ of trials. During error, but not correct, trials the scalp EEG site Cz revealed an evoked potential analogous to the classical signature of error monitoring expected in this task: the ERN ([Figure S6C](#); mean peak amplitude −50–200 ms relative to button press, paired t test $t(11) = 4.53$, $p < 0.001$). The theta power in error trials is significantly stronger than in correct trials ([Figure S6D](#); [0 500]ms relative to button press, 2–10 Hz in frequency, paired t test $t(11) = 6.47$, $p < 0.001$).

Waveform analyses

For each neuron, we extracted the trough-to-peak time as the duration between the first negative peak of the mean waveform ('trough') and the first positive peak after the trough ([Rutishauser et al., 2015](#)). The mean waveform is obtained by averaging all the waveforms assigned to a particular cluster. We normalized the mean waveforms by its maximal amplitude and inverted the waveforms that have the opposite polarity. We considered neurons with a trough-to-peak time < 0.5 ms as 'narrow-spiking' neurons and those > 0.5 ms as 'broad-spiking' neurons.

DATA AND SOFTWARE AVAILABILITY

The spike detection and sorting toolbox OSort was used for data processing, which is available as open-source. Data and custom MATLAB analysis scripts are available upon reasonable request from Ueli Rutishauser (rutishauser@csmc.edu).

Supplemental Information

Single-Neuron Correlates of Error

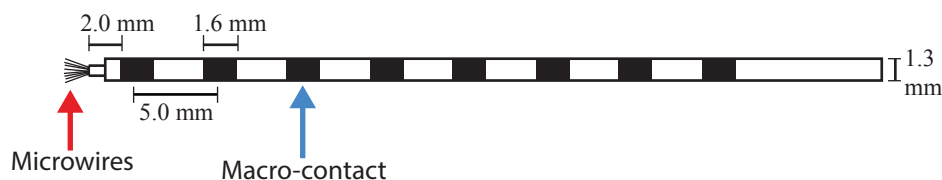
Monitoring and Post-Error Adjustments

in Human Medial Frontal Cortex

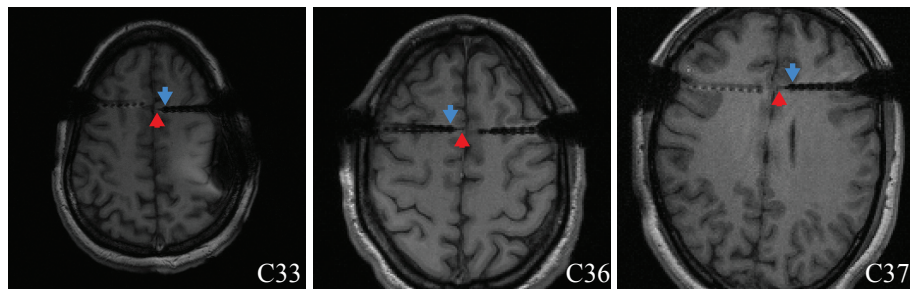
Zhongzheng Fu, Daw-An J. Wu, Ian Ross, Jeffrey M. Chung, Adam N. Mamelak, Ralph Adolphs, and Ueli Rutishauser

Figure S1

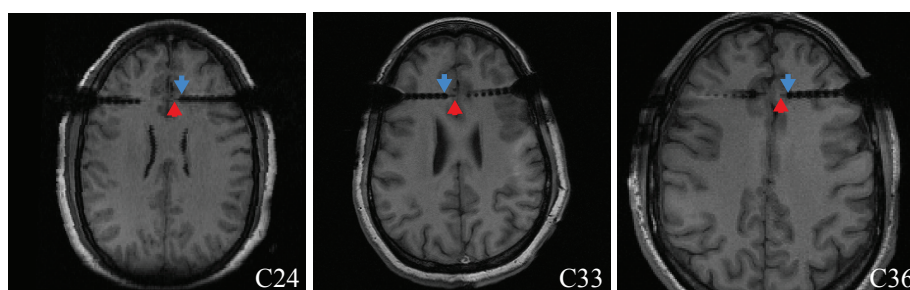
a



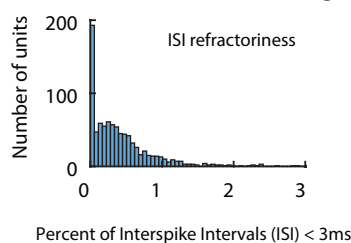
b



c

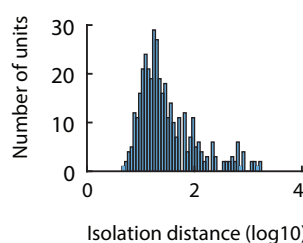


d



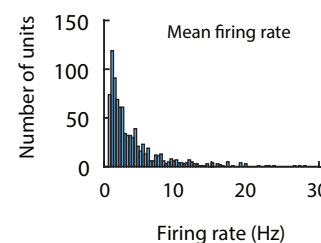
ISI refractoriness

e



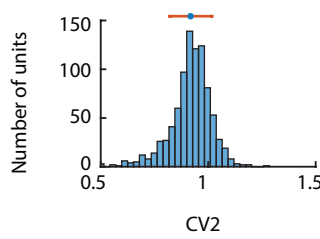
Isolation distance (log10)

f



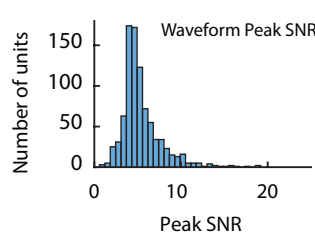
Mean firing rate
Firing rate (Hz)

g



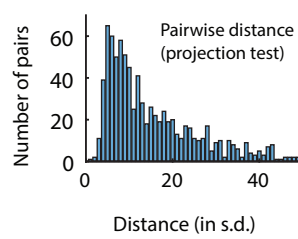
CV2

h



Peak SNR

i



Pairwise distance (projection test)
Distance (in s.d.)

Figure S1. Recording electrode, example post-operative structural MRIs and spike sorting quality. Related to Figure 1-2.

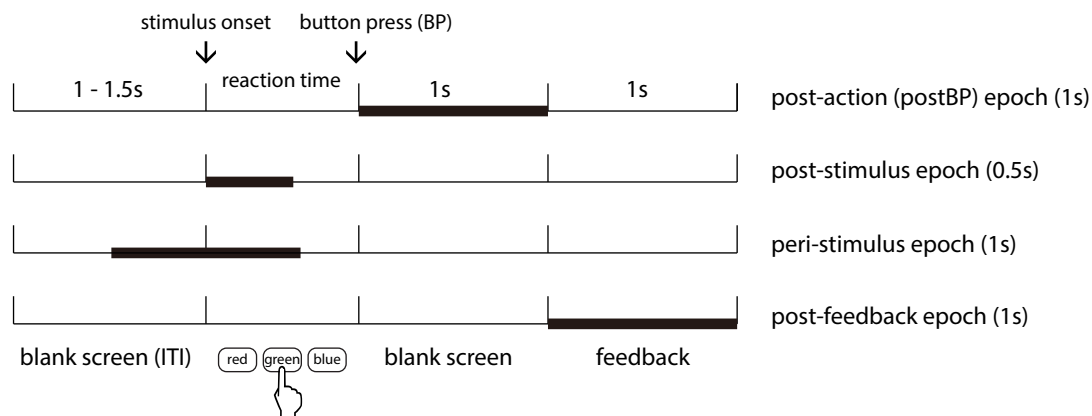
(a) The hybrid macro-micro electrode used. Individual neurons are recorded using high-impedance microwires (red arrow; diameter 40 μ , impedance 400-600k Ω). Field potentials are recorded from the low-impedance (<2k Ω) macro-contact most adjacent to the micro-wires (blue).

(b,c) Example axial T1 MRI scans of recording locations used in pre-SMA (b) and dACC (c). Red and blue arrowheads indicate tips of microwires and the macro contacts used, respectively.

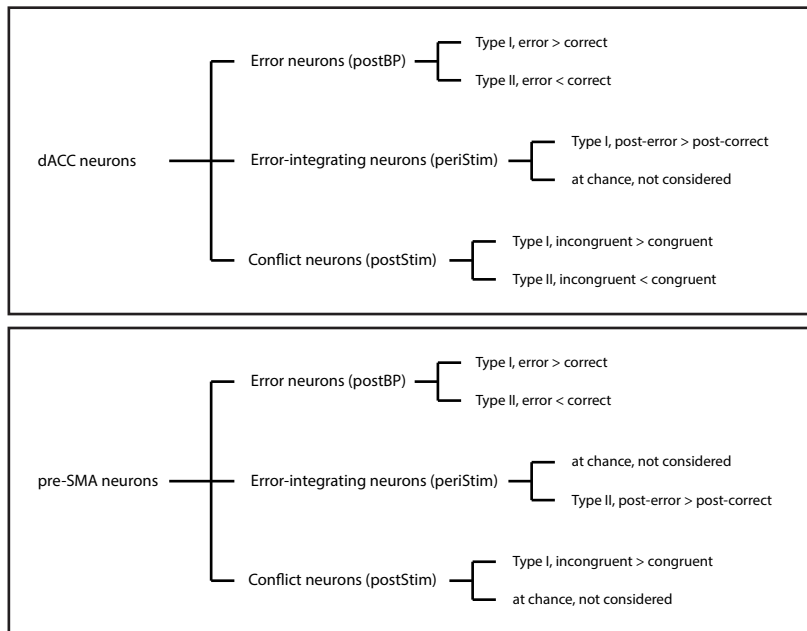
(d-i) Spike sorting quality. Metrics quantifying the individual clusters that we used as putative single-units. (d) Histogram of proportion of inter-spike intervals (ISIs) shorter than 3ms. Most of our recorded clusters had less than 0.5% of their ISIs smaller than 3ms. (e) Isolation distance of all units for which this metric was defined (median 21.5). (f) Histogram of mean spike rates. (g) Histogram of coefficient-of-variation (CV2) values of all units. (h) Histogram of the signal to noise ratio (SNR) of the mean waveform peak computed for each unit. (i) Pairwise distance between all possible pairs, calculated using the projection test (see methods), of units on all wires with at least one cluster isolated. Distance is in unit of standard deviation after normalizing the data such that the distribution of waveforms around their mean is equal to one.

Figure S2

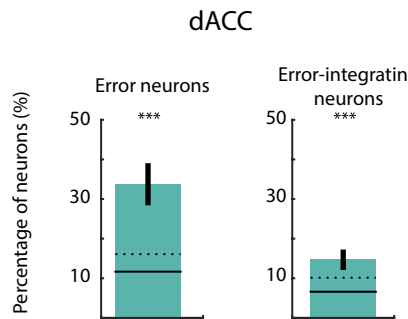
a



b



c



d

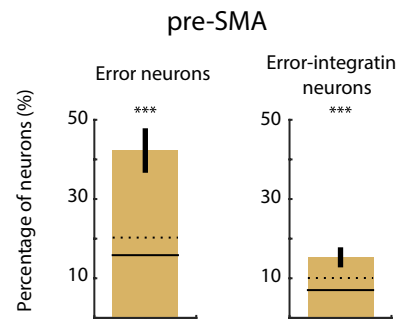


Figure S2. Summary of epochs of interest, neuronal categories and distribution of neuronal categories separately for each session. Related to Figures 2-3.

(a) Epochs used to analyze spiking activity. Thick lines indicate the extent of the time windows. Length of each analysis epoch is indicated in brackets on the right.

(b) Summary of neuronal categories identified in dACC and pre-SMA. The second level lists all neuronal types and the time window (brackets) in which we identified more neurons than expected by chance. The third level lists all sub-types (Type I or II) which were identified at levels higher than expected by chance. The contrasts listed refer to the spike rates during the trial types mentioned (e.g. ‘error > correct’ means spike rates in the error trials were larger than those in the correct trials for this particular type of neurons).

(c-d) Percentage of significant neurons identified in dACC (c) and pre-SMA (d) that qualified as error or error-integrating neurons across recording sessions. Error bars represent \pm s.e.m across sessions, solid and broken horizontal lines, the mean and the 97.5th percentile of the null distribution of the number of neurons expected by chance as estimated using permutation tests.

‘***’ marks groups of neurons which were observed more than expected by chance with p values ≤ 0.001 .

Figure S3

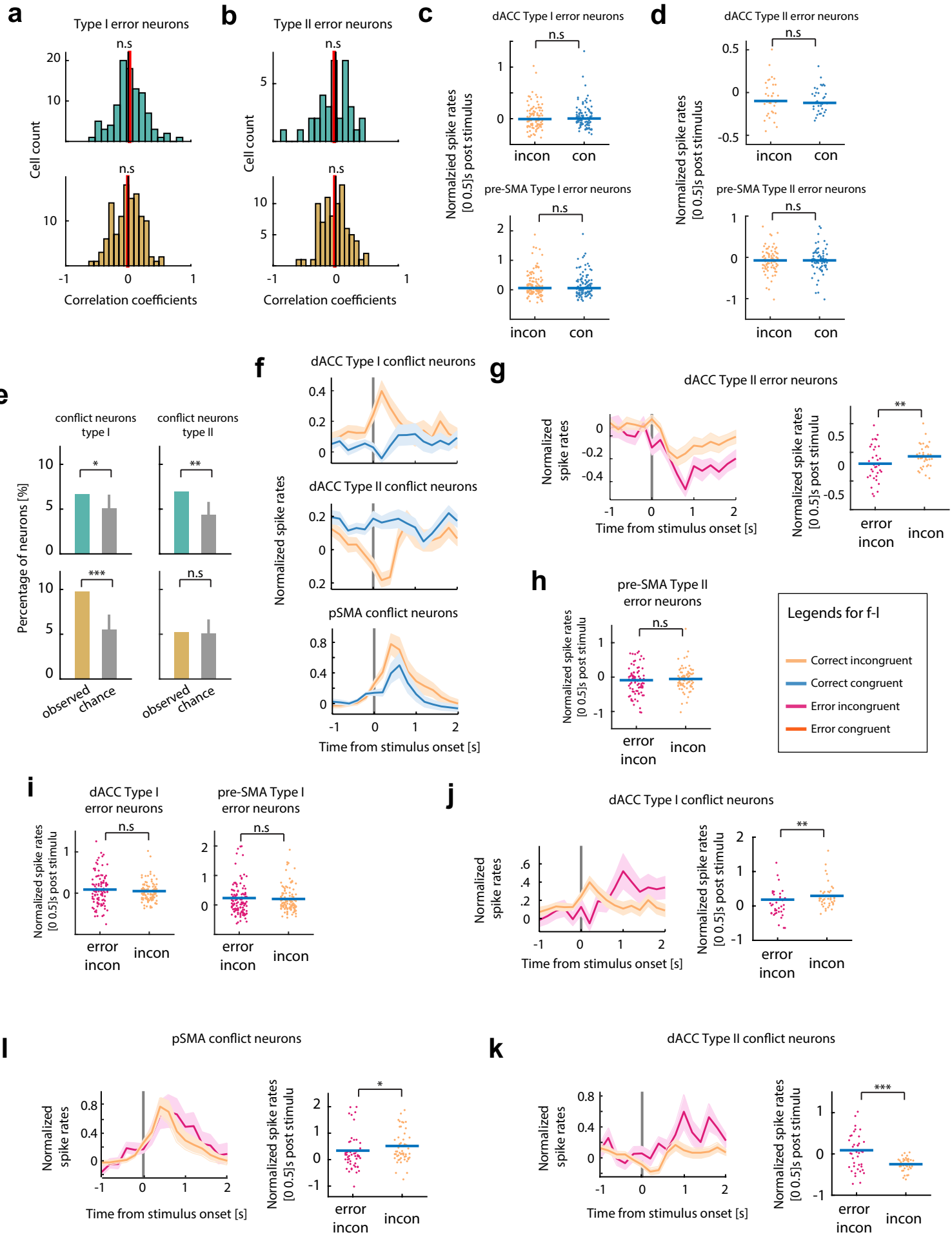


Figure S3. Signatures of conflict and control. Related to Figure 3.

- (a) Correlation between RT and the spike rate of Type I error neurons identified in dACC (top) and pre-SMA (bottom) on the same error trials. There was no significant correlation ($p > 0.04$, $t(98) = 0.86$, t-test) in either area.
- (b) Same as in (a) but for Type II error neurons. There was no significant correlation ($p > 0.05$, $t(117) = -0.41$, t-test) in either area.
- (c) Spike rate of Type I error neurons did not differentiate significantly between correct congruent and incongruent trials in both dACC (upper; $p = 0.92$, z value = 0.1) and pre-SMA (lower; $p = 0.18$, z value = 1.33). Each data point shown is one neuron. Spike rates were quantified within a bin of 500ms size starting at stimulus onset and normalized by the baseline spike rates ([−700 −200]ms relative to stimulus onset). Blue horizontal bars represent median values of the population.
- (d) Same as in (c) but for Type II error neurons. Spike rate of Type II error neurons did not differentiate significantly between correct congruent and incongruent trials in both dACC (upper; $p = 0.61$, z value = 0.51) and pre-SMA (lower; $p = 0.91$, z value = 0.12).
- (e) Number of conflict neurons identified in dACC (green) and pre-SMA (brown). For the definition of Type I and II, see Methods. In dACC, both Type I and Type II conflict neurons have significantly greater number than that is expected by chance ($p = 0.03$ for Type I, $p < 0.001$ for Type II conflict neurons, permutation test). Gray bar shows the mean value of the empirical null distribution. Error bar shows the 95th percentile of the empirical null distribution.
- (f) Average spike rates as a function of time for Type I conflict neurons (top), Type II conflict neurons (middle) in dACC and conflict neurons in pre-SMA (bottom). The spike rates were normalized by the baseline ([−700 −200]ms relative to stimulus onset). Gray bar marks the onset of stimulus.
- (g) Signature of control. Average spike rates as a function of time (left) and within the post-stimulus epoch ([0 500]ms relative to stimulus onset) of Type II error neurons in dACC for error incongruent vs. correct incongruent trials. The spike rates within the post-stimulus epoch differentiated error incongruent and correct incongruent trials significantly ($p = 0.0062$, z value = −2.74). Spike rates were normalized by the baseline ([−700 −200]ms relative to stimulus onset). Gray bar marks the onset of stimulus. Blue bars on the scatter represents median of the population.
- (h) Same as in (g) but for Type II error neurons in pre-SMA. The spike rates within the post-stimulus epoch did not differentiate error incongruent and correct incongruent trials significantly ($p = 0.26$, z value = −1.12).
- (i) Same as in (g) but for Type I error neurons in dACC (left; $p = 0.41$, z value = 0.82, Wilcoxon's signed rank test) and pre-SMA (right; $p = 0.26$, z value = −1.12).
- (j) Same as in (g) but for Type I conflict neurons in dACC. The spike rates within the post-stimulus epoch differentiated error incongruent and correct incongruent trials significantly ($p = 0.006$, z value = −2.75).
- (k) Same as in (g) but for Type II conflict neurons in dACC. The spike rates within the post-stimulus epoch differentiated error incongruent and correct incongruent trials significantly ($p < 0.001$, z value = 3.54).
- (l) Same as in (g) but for conflict neurons in pre-SMA. The spike rates within the post-stimulus epoch differentiated error incongruent and correct incongruent trials significantly ($p = 0.034$, z value = −2.12).
- (c,f) Orange represent correct incongruent trials and blue represents correct congruent trials.
- (g-l) Orange represents correct incongruent trials and magenta represents error incongruent trials.

‘*’, ‘**’, ‘***’ mark groups of neurons which were observed in proportions different than in the overall population with p values ≤ 0.05 , ≤ 0.01 and ≤ 0.001 respectively (for a-b, t-test; for c-d,g-l, Wilcoxon's signed rank test). ‘n.s.’ marks not significant ($p > 0.05$).

Figure S4

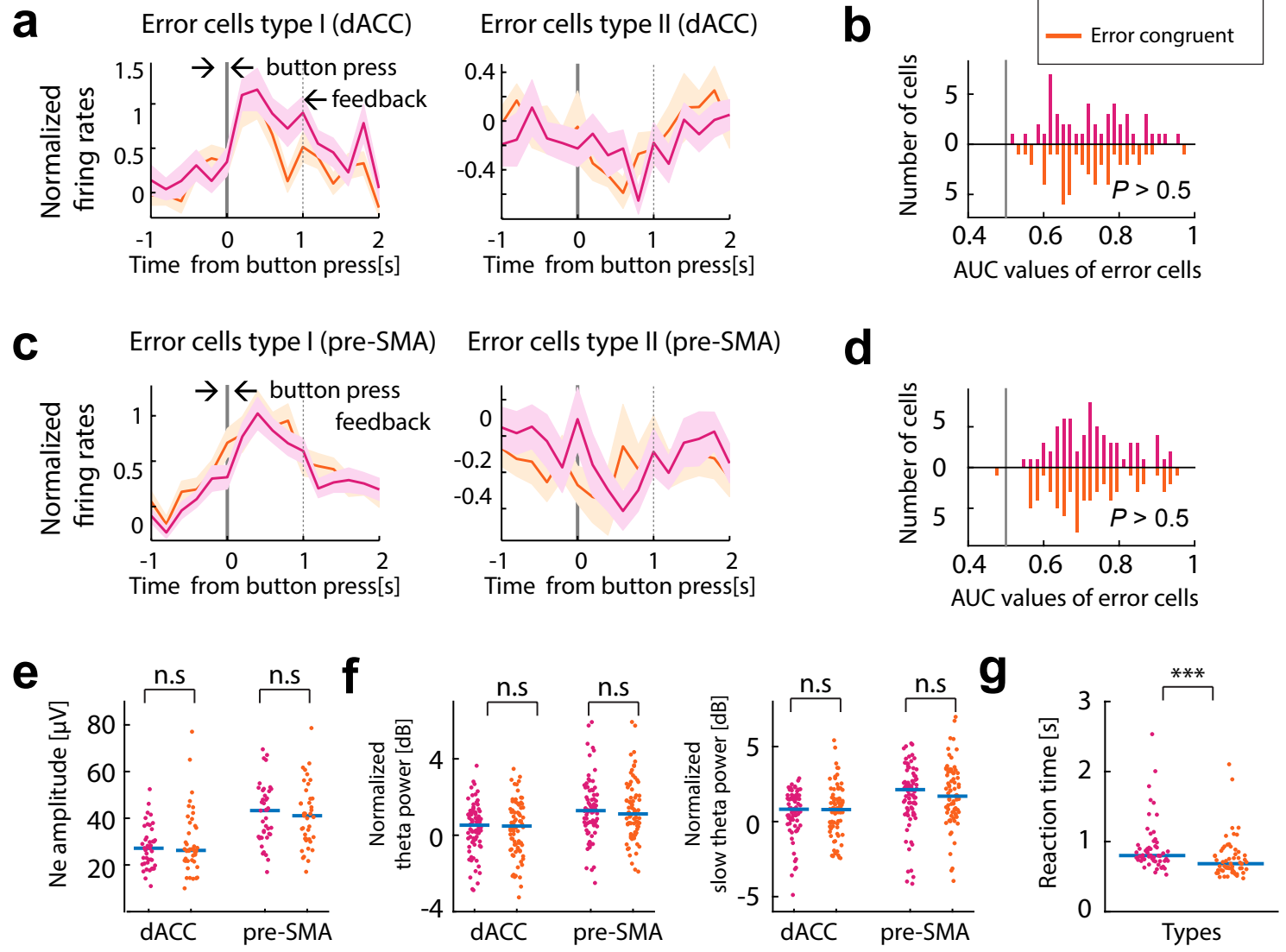


Figure S4. Response of error neurons and the iERN did not differ by error types (congruent error/incongruent error). Related to Figure 3 and 5.

(a) Average spike rates as a function of time for error neurons (Type I and II) in the dACC, normalized by the baseline. Right, Type I error neurons; Left, Type II error neurons. Response is aligned at button press (right). Trials are grouped by congruence (colors; magenta for error incongruent trials and orange for error congruent trials).

(b) Single-neuron ROC analysis of error neurons (both Type I and II) in dACC. The ability of spike rates in the post-button press time window ([0 1]s relative to button press) to differentiate error incongruent and error congruent trials each from correct trials did not differ significantly (AUC values computed from differentiating between correct/congruent error, between correct/incongruent error, 0.59 ± 0.02 vs. 0.58 ± 0.02 in dACC, 0.54 ± 0.02 vs. 0.53 ± 0.02 in pre-SMA; $p > 0.5$ for both areas, Wilcoxon rank sum test).

(c) Same as in (a), but for pre-SMA.

(d) Same as in (b), but for pre-SMA.

(e,f) iERN did not differ between incongruent and congruent errors (iERN amplitude comparisons: $p = 0.8$, $z = 0.25$ for dACC, $p = 0.93$, $z = -0.09$ for pre-SMA, signed rank test. Theta power comparisons: $p = 0.72$, $z = -0.35$ for dACC, $p = 0.93$, $z = -0.09$ for pre-SMA, signed rank test; Slow theta power comparisons: $p = 0.49$, $z = -0.68$ for dACC, $p = 0.19$, $z = -1.3$ for pre-SMA, signed rank test). Shown are the ERN amplitudes (e), theta and slow-theta power (f) for dACC and pre-SMA. Color code, same as in (a-d). Each dot shows one session, horizontal line shows the mean.

(g) The Stroop effect was significant on error trials. Average reaction times in the error incongruent trials were significantly longer than in the error congruent trials ($p < 0.001$, sign rank test).

*** mark statistical comparison with p value ≤ 0.001 . 'n.s.' marks not significant ($p > 0.05$).

Figure S5

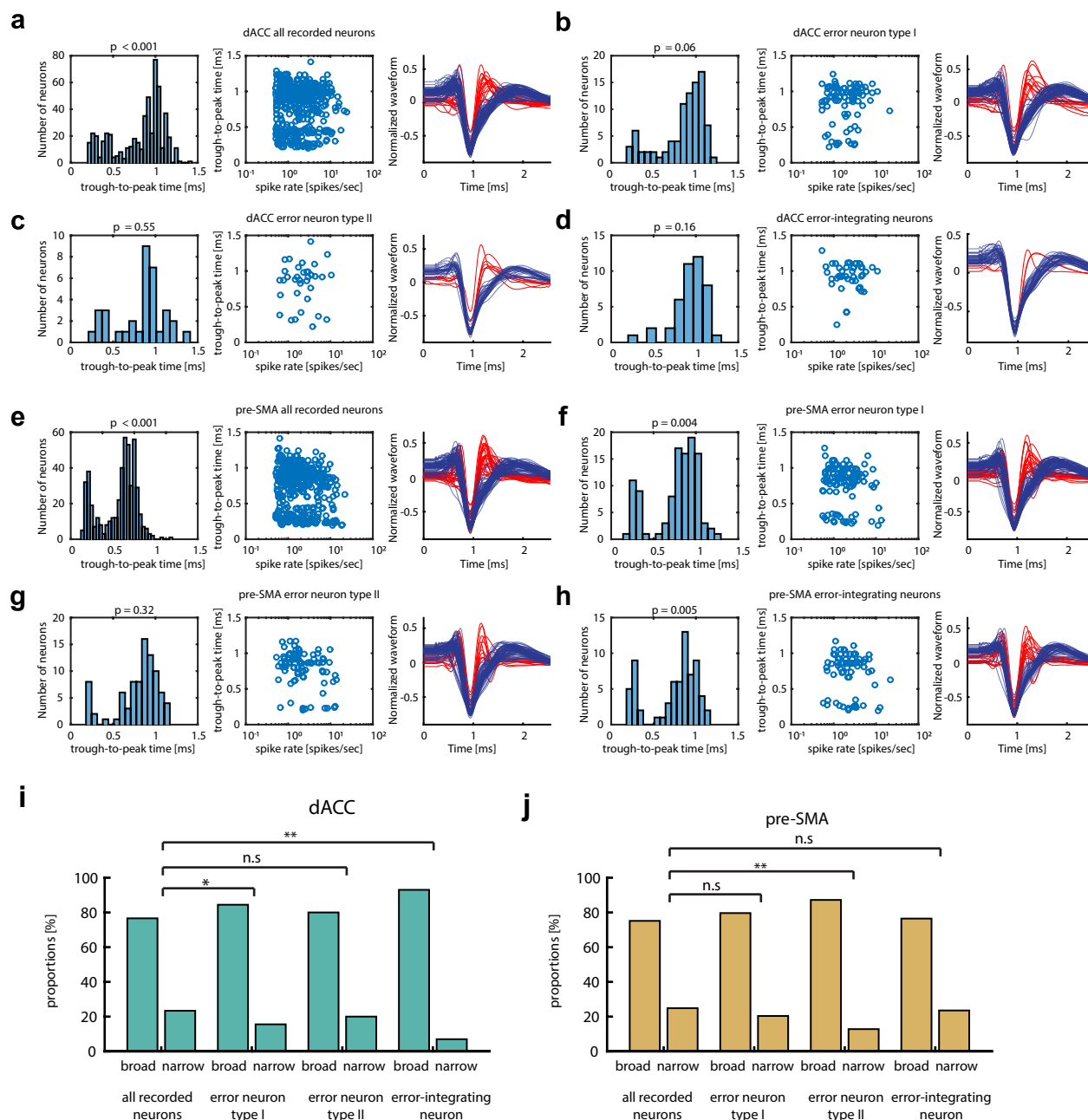


Figure S5. Waveform analyses of error and error-integrating neurons. Related to Figure 2.

(a-h) Distribution of trough-to-peak time (left), trough-to-peak time as a function of spike rates (middle) for each recorded neuron of a given group (described below). The rightmost plot shows the average spike waveforms of all neurons in the group, colored either blue or red depending on whether their trough-to-peak time was longer (blue) or shorter (red) than 0.5ms.

- (a) All recorded neurons in dACC. The trough-to-peak distribution is significantly bimodal ($p < 0.001$).
- (b) All Type I error neurons in dACC. The distribution of trough-to-peak time is not significantly different from unimodal ($p = 0.05$).
- (c) All Type II error neurons in dACC. The distribution of trough-to-peak time is not significantly different from unimodal ($p = 0.55$).
- (d) All error-integrating neurons in dACC. The distribution of trough-to-peak time is not significantly different from unimodal ($p = 0.16$).
- (e) All recorded neurons in pre-SMA. The distribution of trough-to-peak time is significantly bimodal ($p < 0.001$).
- (f) All Type I error neurons in pre-SMA. The distribution of trough-to-peak time is significantly bimodal ($p = 0.004$).
- (g) All Type II error neurons in pre-SMA. The distribution of trough-to-peak time is not significantly different from unimodal ($p = 0.32$).
- (h) All error-integrating neurons in pre-SMA. The distribution of trough-to-peak time is significantly bimodal ($p = 0.005$).
- (i) Proportions of putative pyramidal neurons (trough-to-peak time $> 0.5\text{ms}$) and interneurons (trough-to-peak time $< 0.5\text{ms}$) in dACC. Type I error neurons and error-integrating neurons have a significantly lower proportion of putative inhibitory neurons than the rest of the dACC population (15% and 7% vs 25% in the overall population, $p = 0.05$, odds ratio = 1.81 and $p = 0.0074$, odds ratio = 4.41, respectively; Fisher's exact test).
- (j) Same as in (i) but for pre-SMA. Only the Type II error neurons had a significantly lower proportion of putative inhibitory neurons than the rest of the pre-SMA population (12% vs 26% in the overall population, $p = 0.0034$, odds ratio = 2.58, Fisher's exact test).

'*' and '**' mark groups of neurons which were observed in proportions different than in the overall population with p values ≤ 0.05 , ≤ 0.01 , respectively (Hartigan's dip test). 'n.s' marks not significant ($p > 0.05$).

Figure S6

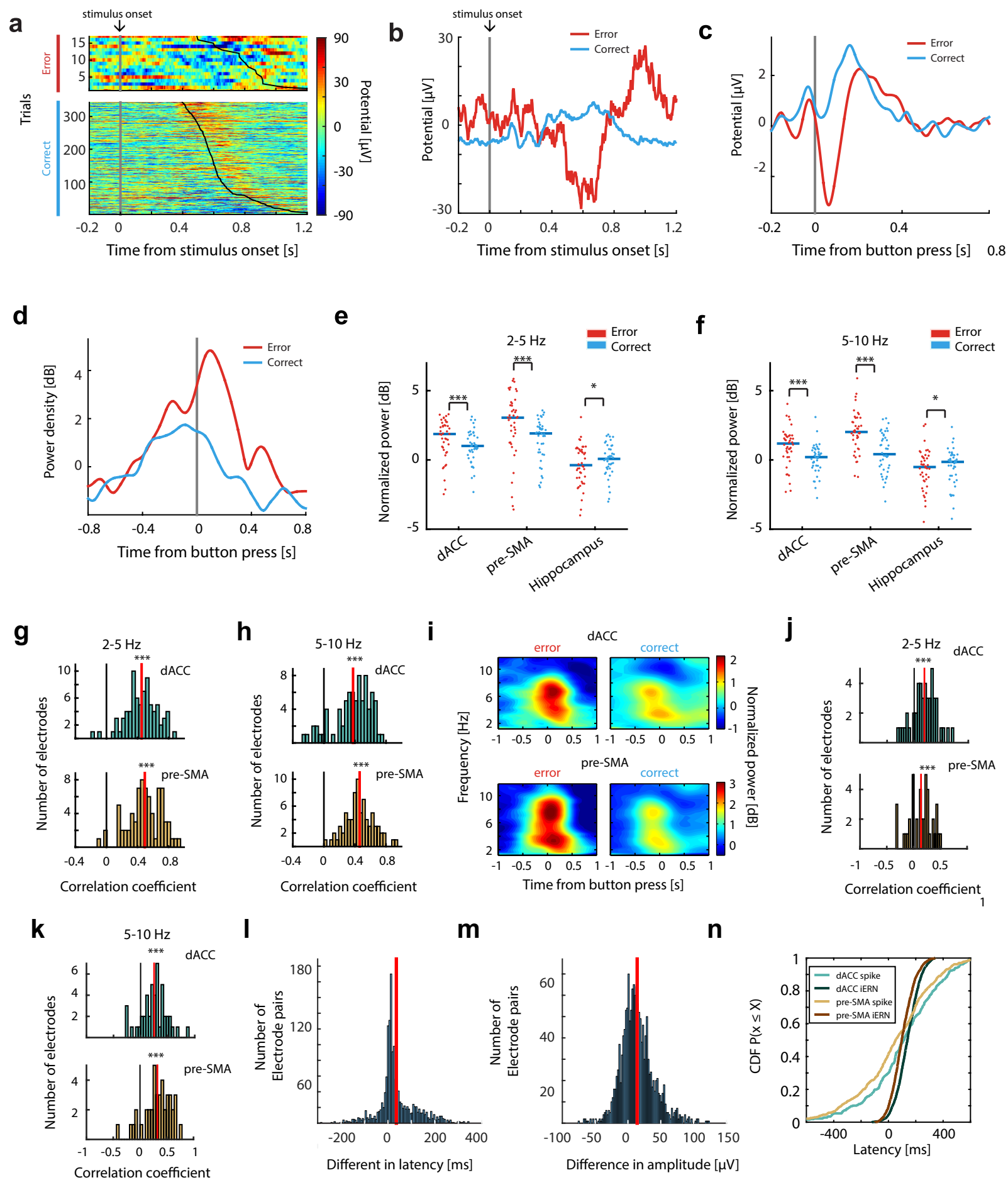


Figure S6. Stimulus-onset aligned intracranial event-related responses, statistics for time-frequency analysis of iERN, and scalp ERN control. Related to Figure 5.

- (a) The same example single-trial event-related potential data as shown in Fig. 5a, but aligned at stimulus onset ($t=0$). The trials were sorted by reaction time (black lines; RT increases from top to bottom) and trial types (upper: error trials, lower: correct trials). Color bar represents ERP amplitude. Note the prominent ERP activities following button press (black line) as well as shortly after stimulus onset (blue). Gray bar represents stimulus onset.
- (b) Average of data shown in (a) by trial types (colors; red for error, green for correct), aligned at stimulus onset ($t = 0$). Note that the sensory-evoked potential did not differ between trial types. Gray bar represents stimulus onset.
- (c-d) Scalp-EEG recordings of non-surgical control subjects ($n = 12$) performing the same task reproduced the classical error-related negativity (ERN) and response-locked theta power (Compare with Fig. 5a-b).
- (c) ERN (negative peak following button press, red) is significantly larger in amplitude in error compared to in correct trials (blue, $t(11) = 4.53$, $p < 0.001$). Gray bar represents button press.
- (d) Theta power as a function of time. Error-related theta power (red) is significantly larger compared to in correct trials (green) after button press ($t(11) = 6.47$, $p < 0.001$). Gray bar represents button press.
- (e) Power in the 2-5Hz band (0 to 500ms following button press) increased significantly more in error trials than in correct trials in both dACC ($p < 10^{-5}$, z value = 6.17) and pre-SMA ($p < 10^{-5}$, z value = 7.3). By contrast, hippocampal theta power also differed, but these differences were of opposite sign ($p = 0.01$, $z = -2.55$ for theta power, $p = 0.01$, $z = -2.56$ for slow theta power). Each dot shows one session, horizontal bar shows mean.
- (f) Same as in (e) but for power in the 5-10Hz band.
- (g) Mean Pearson's correlation coefficients between iERN amplitude and slow theta (2-5Hz) power are significantly larger than zero over all electrodes in dACC (mean correlation = 0.44, $p < 10^{-10}$, $t(78) = 19.2$) and pre-SMA (mean correlation = 0.48, $p < 10^{-10}$, $t(79) = 19.4$, $t(79) = 11.52$, t-test versus 0) Red vertical bars show population means.
- (h) Same as in (g) but for correlations between iERN amplitude and theta (5-10Hz) power in dACC (mean correlation = 0.25, $p < 10^{-10}$, $t(78) = 9.7$) and pre-SMA (mean correlation = 0.33, $p < 10^{-10}$, $t(79) = 11.52$, t-test versus 0).
- (i) Induced theta power, calculated after subtracting the ERP for each condition separately. Spectrograms shown are averaged across all sessions, see panel h for single-session statistics.
- (j) Induced power was significantly correlated with the iERN amplitude in the slow theta (2-5Hz) band in both dACC (mean correlation = 0.21, $p < 10^{-10}$, $t(78) = 8.41$) and pre-SMA (mean correlation = 0.24, $p < 10^{-10}$, $t(79) = 9.02$, t-test versus 0) in pre-SMA.
- (k) Induced power was significantly correlated with the iERN amplitude in the theta (5-10Hz) band in both dACC (mean correlation = 0.25, $p < 10^{-10}$, $t(78) = 9.7$) and pre-SMA (mean correlation = 0.33, $p < 10^{-10}$, $t(79) = 11.52$).
- (l) Latency difference between pairs of iERNs recorded simultaneously in dACC and pre-SMA. The median latency difference of 18ms is significantly different from zero ($p < 10^{-5}$, z value = 19.27, Wilcoxon's signed rank test).
- (m) Amplitude difference between pairs of iERNs recorded simultaneously in dACC and pre-SMA. The median latency difference of 11 μ V is significantly different from zero ($p < 10^{-5}$, z value = 20.14, Wilcoxon's signed rank test).
- (n) Comparisons of spike latencies and iERN latencies (replotting of data shown in main figure on different scale).

'*', '**', ***' mark statistical significance for $p \leq 0.05$, ≤ 0.01 and ≤ 0.001 respectively.

Figure S7

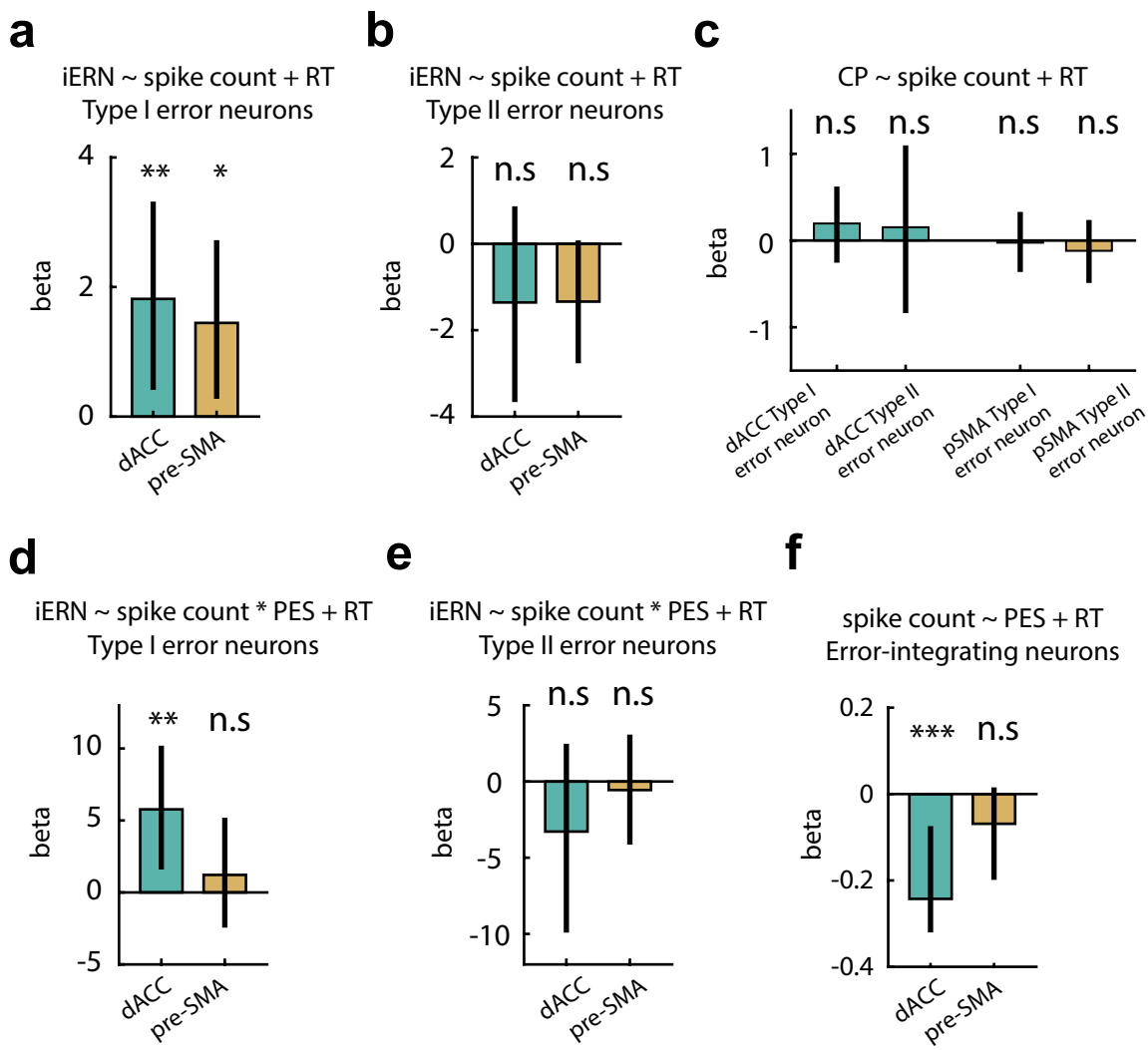


Figure S7. Regression coefficients of GLM models. Related to Figure 6-7.

(a) Regression coefficients for the fixed effect of spike rates (within [0 1]s after button press). The iERN amplitude was significantly correlated with spike of Type I error neurons in both dACC ($p = 0.008, \chi^2(1) = 6.56$, likelihood ratio test) and pre-SMA ($p = 0.012, \chi^2(1) = 5.81$, likelihood ratio test).

(b) Same as in (a) but for Type II error neurons. The iERN amplitude did not correlate significantly with spike rates (within [0 1]s after button press) in dACC ($p = 0.19, \chi^2(1) = 1.64$) and only marginally in pre-SMA ($p = 0.07, \chi^2(1) = 3.36$, likelihood ratio test)

(c) Regression coefficients for the fixed effect of spike rates (within [0 1]s after button press). The CP ('correct potential') was not correlated with the spike rates of any types of error neurons in either dACC (for Type I error neurons, $p = 0.34, \chi^2(1) = 0.92$; for Type II error neurons, $p = 0.74, \chi^2(1) = 0.11$, likelihood ratio tests) or pre-SMA (for Type I error neurons, $p = 0.88, \chi^2(1) = 0.023$; for Type II error neurons, $p = 0.48, \chi^2(1) = 0.49$, likelihood ratio test).

(d) Regression coefficients of the interaction term between the spike rate (within [0 1]s after button press) of the Type I error neurons and PES levels. The correlation between iERN amplitude and the spike rates of the Type I error neurons in dACC was stronger when PES was larger ($p = 0.009, \chi^2(1) = 6.56$, likelihood ratio test). The same relationship did not hold significantly for Type I error neurons in pre-SMA ($p = 0.5, \chi^2(1) = 0.44$, likelihood ratio test).

(e) Same as in (d) but for Type II error neurons. The strength of correlation between iERN amplitude and the spike rates of the Type II error neurons did not vary significantly between PES levels in either dACC ($p = 0.67, \chi^2(1) = 0.18$, likelihood ratio test) or pre-SMA ($p = 0.48, \chi^2(1) = 0.5$, likelihood ratio test).

(f) Regression coefficients of the fixed effect of PES levels. The spike rates of the error-integrating neurons were strongly correlated with PES in dACC ($p < 0.001, \chi^2(1) = 15.76$, likelihood ratio test), but only marginally so in pre-SMA ($p = 0.07, \chi^2(1) = 3.31$, likelihood ratio test).

Error bars represent 95% confidence interval obtained from parametric bootstrapping. '**', ***, *** mark statistical significance with p values $\leq 0.05, \leq 0.01$ and ≤ 0.001 respectively using the likelihood ratio test. 'n.s' marks not significant ($p > 0.05$).

Supplementary Tables

Table S1. Subjects recorded. Related to Figure 1.

List of all subjects recorded.

ID	Sex	Age	Epi Diagnosis	Macro recording performed	Sessions performed
H11	M	16	right lateral frontal	N	2
H14	M	31	Bilateral indep. Temporal	N	2
H16	F	34	right frontal	N	2
H17	M	19	left inferior frontal	N	3
H18	M	40	Right temporal	N	1
H19	M	34	Left frontal	N	1
H21	M	20	Not localized	N	2
H28	M	23	Right mesial temporal	N	1
H31	M	30	Right temporal	N	1
H41	M	19	Right posterior temporal	N	1
H42	M	29	Not localized	N	1
H49	F	54	Right amygdala and hippocampus	N	2
C24	F	47	Not localized	N	2
C25	F	36	Bilateral indep. Temporal	N	2
C26	F	56	Right temporal	N	1
C27	M	45	Left temporal	N	1
C29	M	19	Left temporal neocortical	N	4
C31	M	31	Left temporal neocortical	N	3
C32	M	19	Not localized	N	1
C33	F	44	Right temporal	N	4
C34	M	70	Bilateral temporal	N	5
C35	M	63	Left temporal neocortical	Y	6
C36	M	45	Right Hippocampus	Y	6
C37	F	33	Right Hippocampus	Y	11

C39	M	26	Right insula	Y	6
C40	M	25	Right motor cortex	Y	4
C42	F	25	Not localized	Y	5
C47	M	33	Right mesial temporal	Y	2
C48	F	32	Left medial temporal	Y	1

Table S2. Percentage and average spike rate of neurons. Related to Figures 2-3.

Summary of percentages and average spike rates (\pm s.d.) of neuronal categories. Neurons of the types marked as “NA” were found not more than expected by chance.

dACC	Error neurons		Error-integrating neurons	
Types	I	II	I	II
Spike rate (Hz, \pm s.d)	2.61 \pm 2.8	3.24 \pm 2.2	2.77 \pm 2.1	NA
Percentage (%)	24.8	8.8	11.9	NA

pre-SMA	Error neurons		Error-integrating neurons	
Types	I	II	I	II
Spike rate (Hz, \pm s.d)	2.47 \pm 2.3	3.6 \pm 3.3	NA	3.47 \pm 3.6
Percentage (%)	27.4	18.6	NA	13.6

Table S3. Percentage of overlap between neuron types. Related to Figures 3, S3

Summary of proportions of neurons in the overlap between error neurons and conflict neurons. The overlap was tested with Fisher’s exact test. Example of how to read this table: the first entry below shows that “In dACC, out of all conflict neurons type I, 24.4% are also error neurons Type I”.

dACC	Percentage in: Conflict neuron Type I	Percentage in: Conflict neuron Type II
Error neuron Type I	24.4%	23.3%

Error neuron Type II	8.6%	7%
----------------------	------	----

dACC	Percentage in: Error neuron Type I	Percentage in: Error neuron Type II
Conflict neuron Type I	10%	7.3%
Conflict neuron Type II	10.1%	8.6%

dACC	Conflict neuron Type I	Conflict neuron Type II
Error neuron Type I	$p = 0.18$, odds ratio = 1.77	$p = 0.19$, odds ratio = 1.65
Error neuron Type II	$p = 0.50$, odds ratio = 1.34	$p = 0.73$, odds ratio = 1.27

Pre-SMA	Percentage in: Conflict neuron Type I
Error neuron Type I	27.8%
Error neuron Type II	20.4%

Pre-SMA	Percentage in: Error neuron Type I	Percentage in: Error neuron Type II
Conflict neuron Type I	12.7%	13.8%

Pre-SMA	Conflict neuron Type I
Error neuron Type I	$p = 0.224$, odds ratio = 1.48
Error neuron Type II	$p = 0.22$, odds ratio = 1.59